Meso-scale modelling of the thermo-mechanical response for concrete with complex-shaped aggregates in early age

Wenjing Qiu[a], Ji-Hua Zhu[a], ShaoJun Fu[b,*], ChaoQun Zeng[c], Jianqiao Ye[d]

[a] *Guangdong Province Key Laboratory of Durability for Marine Civil Engineering, College of Civil and Transportation Engineering, Shenzhen University, Shenzhen, China*
[b] *School of Civil Engineering, Wuhan University, Wuhan 430072, China*
[c] *School of automobile and transportation, Shenzhen polytechnic, Shenzhen, China*
[d] *Department of Engineering, Lancaster University, Lancaster LA1 4YR, UK*

Abstract: Self-restraint stress produced in early age is a matter of interest associated with cracking of concrete. Mesoscopic modelling nowadays is one of the effective approaches to investigate internal stresses, deformation, damage of concrete at much smaller scale. However, grid discretization and mesoscopic properties calibration are still challenging issues that prevent fast pre-processing and require extremely dense meshes for accurate solutions. In this paper, a thermo-mechanical model required only regular-element discretization is proposed by developing a diffuse meshing technique to analyze the evolution of self-restraint stress. Cross-scale numerical validations are carried out to calibrate the mesoscopic parameters, along with verifying the feasibility of the proposed model. Furthermore, the effect of simplified aggregate mesostructure on the thermo-mechanical behavior of concrete is evaluated through comparisons with the results obtained by considering complex-shaped aggregate using the proposed diffuse element model. The results show the thermo-mechanical mismatch between different components is the main reason for producing the self-restraint stress, and aggregate meso-structure have nonnegligible influence on the global response or local behavior.

Keywords: concrete mesoscopic model; self-restraint; aggregate morphology; orientation; diffuse meshing

1. Introduction

Concrete is the most widely used material in the world with extensive applications, and the durability of concrete is strongly related to its thermo-mechanical process. Cracking in most mass concrete structures in service life is attributed to the tensile stress that is generated not only from external load but also the restrained internal deformation. For instance, in the process of concrete hydration or under artificial cooling conditions, a significant temperature gradient will be produced between the edge and the center of a mass concrete, where self-restraint tensile stress will inevitably emerge even in the absence of external constraints or loads [1-3]. The tensile stress may induce initial damage or micro-cracks inside the concrete, which adversely affects its mechanical properties and durability. In the normal service stage of a concrete structure, the initial micro-cracks are prone to develop into macro cracks under the combined action of self-restraint tensile stress and external load. It has been recognized that the development of early self-restraint stress has a strong correlation with crack sensitivity.

---

[*] Corresponding author.
  E-mail addresses: wenjingqiu@szu.edu.cn (W.J. Qiu), sgjg@whu.edu.cn (S.J. Fu）

Physical experiment is one of the most traditional approaches to obtain macroscopic mechanical properties of concrete, while it has strong dependence on experimental equipment, environment and specimens [4]. Thus, experimental results often show significant discrepancies, especially, in the study of the internal mechanism of such a heterogeneous materials. A macroscopic numerical analysis often simulates concrete as a homogeneous material and fails to capture the evolution of internal stresses. With the progress of computer technology and the development of numerical methods, mesoscopic modeling based on Finite Element Method (FEM) provides an effective way to study mechanical behavior of concrete, known as the concept of ''numerical concrete'' [5-7]. As a multi-phase heterogeneous composite material, the complex macroscopic mechanical behavior of concrete is the reflection of its mesoscopic structure. In this case, the internal interactions between different components of concrete, i.e. mortar matrix and aggregates, are required to be considered properly and the influence of the multi- phases in concrete on the macroscopic properties also need to be investigated [8]. At meso-level, the mismatched thermal expansion and deformation between different components, primarily mortar matrix and aggregates [9,10], cause internal restraint and in turn induce self-restraint stress that involves a complex coupling process from heat transfer to stress-strain response. Over the past few decades, several useful models have been proposed to numerically analyze thermo-mechanical behavior of concrete. Fu et al. [11] proposed a 2D mesoscopic thermo-elastic damage model to study the thermal cracking under elevated temperature. Xotta et al. [12] numerically studied the performance of concrete under elevated temperature with a 3D meso-scale model. Zunino et al. [13] used a two-phase mesoscopic model to assess the thermo-mechanical micro-cracking damage for early-age concrete. Sinaie et al. [14] investigated the damage caused by temperature by using the discrete element method. The model proposed by Xu et al. [15] accounted for time-dependent properties of mortar, and confirmed that it has a marked impact on the self-restraint stress evolution in young concrete. Nguyen et al. [16] adopted a lattice framework to study the effect of thermal conductivity on thermo-mechanical behavior of concrete. Caggiano et al.[17,18] presented a coupled thermo-mechanical interface model and investigated meso-scale response of concrete under high temperature. However, those analytical models ignored the complex morphology of actual aggregates by using a simplified geometry, which is unlikely to exhibit what really happened in the interior concrete.

It is generally recognized that the morphology and orientation of coarse aggregate have a no-negligible influence on the mechanical properties of concrete at meso-level [19, 20]. The surface roughness, equidimensionality and angularity of aggregates greatly affect the mechanical occlusion and interaction between aggregates and cement matrix, thus affecting the bearing capacity and damage distribution of concrete. Using a mesoscopic model with spherical aggregates may deviates from the actual situation. The main question here is what is the impact of such simplified mesostructure on the accuracy of the simulated results. To answer this question, reconstruction of realistic-looking aggregates is an essential step in the construction of a more realistic mesoscopic model of concrete. To date, reconstructing a meso-scale aggregate based on geometric algorithms can be roughly divided into two categories: the image-dependent and image-independent methods [21]. Compared to an image-dependent method, an image-independent method, which uses a function to represent a geometry on the basis of a known point set and is termed also as a surface reconstruction method, is more computational cost-effectivewith higher productivity and less restriction on image resolution. Furthermore, the implicit T-spline surface reconstruction algorithm is superior in reducing noises and utilizing incomplete data to describe a complexed topology [22, 23]. Therefore, it provides an effective approach to reconstruct realistic-looking aggregates.

Numerical calculations by using FEM require discretization of multi-phase components in a mesoscopic model to characterize the heterogeneity of concrete. The meshing, whose quality greatly restricts the accuracy of numerical results, is one of the main issues that have to be addressed in a mesoscopic simulation. It is still a difficult operation to mesh a complex meso-structure with a high aggregate volume content [24, 25]. At present, two kinds of meshing methods for a mesoscopic model are available, i.e., the direct division method and the indirect division method. The

direct division method is generally used in two-dimensional cases. For three-dimensional cases, Xu et al. [4] divided aggregates and concrete, respectively, into tetrahedral patches to obtain two group point sets that were subsequently merged to regenerate a new point set. An algorithm called 'Incremental Topological Flipping' [26] and the method of inserting line segments into tetrahedral patches [27] were used then to achieve the meshing of each components. This method can successfully mesh a mesoscopic model with aggregates of regular geometry. However, the pre-process is practically applicable in generating complex-shaped aggregates. To address this problem, the indirect division method is preferred to discretize a mesoscopic model. The mapping mesh method [28], by which the material of element is determined by the component that possess more than half of the nodes of the element, is used for numerical calculation. This method apparently has no limitation on the morphology of aggregates. Clearly, this method ignores the geometry of the interface between aggregate and matrix and inevitably introduce additional errors. In order to improve the solution, the diffuse meshing method is developed [29], whereby cement matrix and aggregates properties are projected on the shape functions of the finite element mesh. It serves to represent different concrete component in one finite element without meshing explicitly for the complex-shaped aggregate. However, to the authors' best knowledge, evolution of self-restraint stress when diffuse meshing method is used in a mesoscopic model has rarely been discussed in the published literatures.

The accuracy and predictive ability of such meso-scale models is strongly tied to the thermo-mechanical behavior of both aggregate and cementitious materials [15]. Since it is difficult to directly measure these time-dependent parameters accurately for the numerical model, calibration of these mesoscopic time-dependent parameters from the commonly-used homogeneous concrete material parameters determined by macro-experiment is an alternative approach to follow. Nguyen-Sy et al. [30-32] proposed a homogenization method to predict the elastic properties of cementitious material. However, calibration of the time-dependent parameters of cement, such as adiabatic temperature, creep and autogenous volume deformation, have been rarely made in the published literatures.

To facilitate the pre-process, a novel thermo-mechanical modelling framework with regular-element discretization is presented to investigate the evolution of self-restraint stress in this paper. This model, which combines the diffuse meshing technology with the theory of linear viscoelasticity, takes into consideration of the effects of time-dependent behavior of cementitious materials, including adiabatic temperature rise, creep strain and autogenous volume deformation. In this study, it is assumed that the concrete is always elastic in the early age. The transition of material properties across an aggregate/matrix interface is approximately projected into a liner transition zone, the thickness of which depends on the closet distance between the Gaussian point across the interface. This is followed by single factor validation for cross-scale numerical simulation. The results of the proposed mesoscopic model are compared with the results from the homogeneous concrete model obtained by FEM to calibrate the mesoscopic parameters. A good agreement between the simulation results of above two models and theoretical solution of experimental result is evidenced, indicating that the proposed model is capable to interpret the thermo-mechanical mechanism during early-age hydration. To investigate the effect of simplified aggregate mesostructure, several equal volume aggregate models with complex morphology and different orientations are established by using the implicit T-spline algorithm. Compared to the results of the spherical aggregate model, the impact of aggregate mesostructure on the thermo-mechanical behavior of concrete is further studied and discussed.

2. Mesoscopic thermo-mechanical model

2.1. Generation of the meso-structure

The aggregate model of complex shape is constructed by using the implicit T-spline surface reconstruction algorithm [33-35]. The implicit surface can be represented as the zero-level set of sign functions. Thus, the mathematical expression of the implicit T-spline surface based on the known point sets $\{p_i(r_i, s_i, t_i)\}_{i=1}^n$ is defined

as:

$$f(r,s,\text{t}) = \frac{\sum_{i=1}^{M} c_i B_i(r, s, t)}{\sum_{i=1}^{M} B_i(r, s, t)} = 0, (r,s,t) \in \Omega \tag{1}$$

where c_i is the coefficient of the i-th control point, $B_i(r,s,t) = N_{i0}^d(r) * N_{i0}^d(s) * N_{i0}^d(t)$. $N_{i0}^d(r)$, $N_{i0}^d(s)$ and $N_{i0}^d(t)$ are the B-spline basis functions with the homologous knot vectors $r_i = [r_{i0}, r_{i1}, \dots, r_{id+1}]$, $s_i = [s_{i0}, s_{i1}, \dots, s_{id+1}]$ and $t_i = [t_{i0}, t_{i1}, \dots, t_{id+1}]$.

The tangible function can be determined by adding off-surface point sets $\{p_i(r_i, s_i, t_i)\}_{i=n+1}^{N}$ whose implicit function values f are not zero:

$$f(r_i, s_i, t_i) = \begin{cases} 0, i = 1,2,\dots,n \\ d_i, i = n+1, n+2, \dots N \end{cases} \tag{2}$$

where d_i is the sign distance from the i-th off-surface point to the nearest patch of surface.

A custom sinusoidal generatrix function, of which the amplitude parameter represents the aggregate size and the period parameter defines the aggregate flatness, is used to auto-generate point sets of gravel aggregate. The point sets of crushed aggregate are obtained by defining the damage-degree parameter, i.e., the number of cut-plane. Combined with the reconstruction algorithm, a realistic-looking aggregate (Fig.1) is be constructed subjected to the above-mentioned controlling geometric parameters. To better specify the shape and the random packing position of an aggregate, some geometric transformations of the constructed aggregate, such as translation, rotation and scaling (aspect ratio), are performed to generated a new aggregate by substitution method.

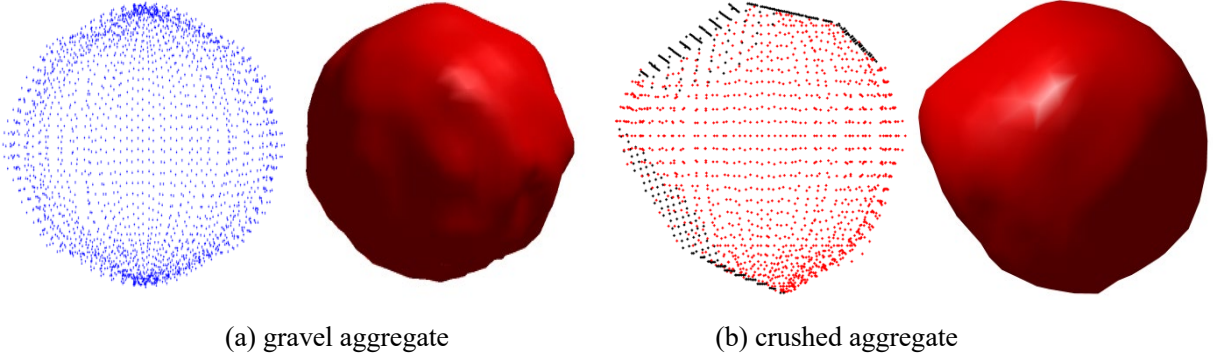(a) gravel aggregate   (b) crushed aggregate

Fig.1. Samples of different types of aggregate point sets and models

Furthermore, the meso-structure, namely the Random Aggregate Model (RAM), is established by using the proposed packing method that improves the occupation and removal method [36] by combining with the layering disposition method [37]. The detailed procedure of generating meso-structure models with complex-shaped aggregates can be found in the previous study [38].

In order to assess the impacts of using simplified mesostructure, including the morphology and orientation of aggregate, on the thermo-mechanical behavior, two groups of RAMs with different aggregate shapes but the same content are firstly established. One is to use implicit T-spline reconstruction algorithm to describe the complicate morphology of real aggregates. The second aggregate model is simply represented by an equivalent sphere of the same volume as the counterpart in the T-spline constructed model. Concrete anisotropy can be measured with respect to the casting direction, thus four directions of aggregates are discussed in this paper. The aggregates to be considered are crushed aggregates with a flatness of 8 and degree of damage (cut-plane number of crushed aggregates) from 6 to 10. The dimension of the sample is 150mm*150mm*150mm. The above model building approach is summarized as follows:

(1) Assuming that the gradation of aggregate follows the Fuller gradation curve, generate the initial random spherical aggregate model by previous proposed packing method and record the coordinates of the spherical center and radius of each aggregate.

(2) Generate crushed aggregate model by taking the radius of each aggregate in the initial random spherical aggregate model as the maximum particle size of each crushed aggregate, and then regenerating new aggregates by using the implicit T-spline algorithm at the position of the spherical centers of each aggregates in the initial random spherical aggregate model. Thus, the spherical aggregates generated in Step (1) is the circumscribed sphere of the aggregates with complex shape, as shown in Fig.2(b) (Model II).

(3) Generate the spherical aggregate model by calculating the volume V of each aggregates in Model II to obtain the equivalent radius ($R = \sqrt[3]{3V/4}$) of the spherical aggregates in this model, as shown in Fig.2(a) (Model I).

(4) Rotate each aggregates in Model II 90°, 180° and 270° counterclockwisely around the z-axis, respectively, to regenerate new mesoscopic models, as shown in Fig.2(c) (Model III), Fig.2(d) (Model IV) and Fig.2(c) (Model V). The aggregate function after rotation can be written as $f(r * \cos\theta - s * \sin\theta, r * \cos\theta + s * \sin\theta, t) = 0$ (θ is the rotated angle) through substitution.

It can be found from Fig.3 that the grading curve of the initial random spherical aggregate model generated by Step(1) is very close to the target curve (Fuller grading curve). After following the above modelling process, the content of aggregates of Model I ~ Model V is reduced (28.67%), and the aggregate weight percentage in the middle of each gradation of these models are more than that of the initial random spherical aggregate model due to the radius reduction of each aggregate (Fig.3). However, this is not the main concern of the current work. Obviously, the approach can ensure that the aggregates of the five models are not overlapped and the five models have the same content and spatial distribution of aggregates. Thus, the main factor that causes difference in the numerical results is the influence of aggregate morphology or orientation.
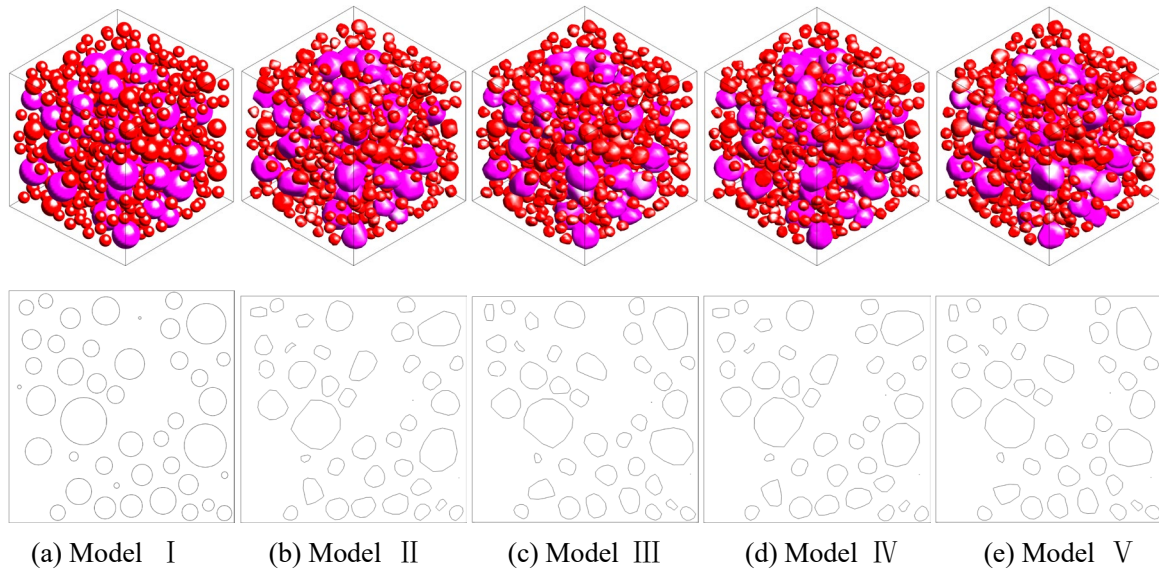

(a) Model Ⅰ   (b) Model Ⅱ   (c) Model Ⅲ   (d) Model Ⅳ   (e) Model Ⅴ

Fig.2. The five microscopic models and the corresponding microstructures of intermediate sections
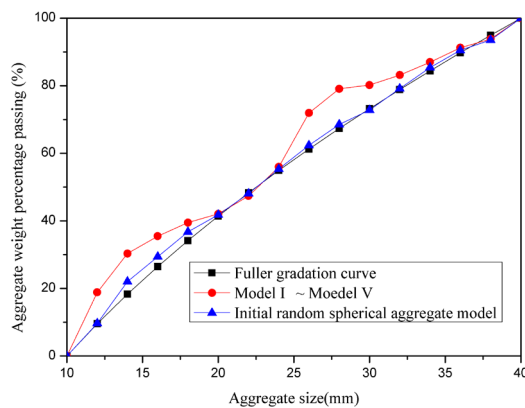
Fig. 3. Comparison of gradation curves

2.2. Heat transfer

For a homogeneous and isotropic object, the heat absorbed in the process of temperature rising should be equal to the sum of the heat from the outside and inside sources [39]. The heat conduction equation of thermal movement can be expressed as follows:

$$\frac{\partial T}{\partial \tau} = a \left(\frac{\partial^2 T}{\partial x^2} + \frac{\partial^2 T}{\partial y^2} + \frac{\partial^2 T}{\partial z^2} \right) + \frac{1}{c\rho} \frac{\partial Q}{\partial \tau} \tag{3}$$

where T is temperature; $a = \frac{\lambda}{c\rho}$ is thermal diffusivity, in which λ is thermal conductivity, c is specific heat of material, ρ is density, τ is time and Q is released heat in unit volume of material.

As for a microscopic concrete model, it is widely considered that only cement matrix can produce hydration heat, resulting in producing temperature gradient between two components. The hydration heat of cement is regarded as a function of age. In this paper, the following exponential relationship is employed [40]:

$$Q(\tau) = Q_0/(n+\tau) \tag{4}$$

where $Q(\tau)$ is the cumulative hydration heat per unit mass of cement at age τ, Q_0 denotes the final hydration heat when $\tau \to \infty$, and n is an experimentally determined material parameter.

Introducing Eq. (4) into Eq. (3) and considering initial and boundary conditions result in a unique solution to Eq. (3). The boundary condition when the surfaces of concrete is exposed to the air can be derived from the Newton's cooling law [39, 41] below.

$$q = -\lambda \frac{\partial T}{\partial n} = \beta (T_c - T_a) \tag{5}$$

where q is the heat flux through concrete surface per unit area, β is convection coefficient, T_c and T_a are the temperature of concrete surface and air, respectively.

2.3. The constitutive model

Since stress evolution of the laboratory-sized concrete in the standard environmental curing process is studied in this paper, the temperature gradient between the center and outside of the sample is relatively small, and the concrete is considered to be elastic in the whole curing process. On the linear viscoelasticity [42], the strain $\varepsilon(t)$ at time t [1] can be written as the sum of the instantaneous elastic strain $\varepsilon_e(t)$, the thermal strain induced by temperature variations $\varepsilon_T(t)$, the creep strain $\varepsilon_C(t)$ and the autogenous volume strain $\varepsilon_g(t)$:

$$\varepsilon(t) = \varepsilon_e(t) + \varepsilon_T(t) + \varepsilon_C(t) + \varepsilon_g(t) \tag{6}$$

It is assumed that the aggregates are entirely elastic, while the cement matrix possesses age-dependent properties in the proposed model. The mechanical parameters of the matrix materials, including elastic modulus, creep and autogenous volume deformation, increase continually with the degree of hydration and, hence, regarded as functions of age [1, 40].

(1) Elastic strain

According to the linear constitutive law, when a concrete is subjected to stress $\sigma(\tau)$ at age τ, the instantaneous elastic strain is defined as：

$$\varepsilon_e(t) = \int_{t_0}^{t} E^{-1}(\tau) \frac{\mathrm{d}\sigma(\tau)}{\mathrm{d}\tau} \mathrm{d}\tau \tag{7}$$

where $E(\tau)$ is the instantaneous elastic modulus (sixth order tensor) of concrete at age τ, and t_0 is the age at the beginning of loading.

The evolution of elastic modulus of concrete can be expressed as:

$$E(\tau) = E_0\tau/(a+\tau) \tag{8}$$

where E_0 is the final elastic modulus of concrete as age $\tau \to \infty$, and a is the semi-coagulation age.

(2) Thermal strain

The relation between the thermal strain $\varepsilon_T(t)$ and the temperature increment ΔT [1, 39, 43] is

$$\varepsilon_T(t) = \alpha_T \Delta T \tag{9}$$

where α_T is coefficient of linear thermal expansion (CLTE).

(3) Creep strain

The constitutive relation of material creeping is:

$$\varepsilon_C(t) = \int_{t_0}^{t} C(t,\tau)\frac{\mathrm{d}\sigma}{\mathrm{d}\tau}\mathrm{d}\tau \tag{10}$$

where $C(t,\tau)$ is the creep compliance defined by a series of Kelvin chains [1]:

$$C(t,\tau) = \sum_{j=1}^{m} \phi_j \left(1 - e^{-r_j(t-\tau)}\right) \tag{11}$$

For recoverable creep (short-term creep) and irrecoverable creep (long-term creep), ϕ_j are defined, respectively, as

$$\phi_j = f_j + g_j\tau^{-p_j} \tag{12}$$

$$\phi_j = g_j\tau^{-r_j} \tag{13}$$

where f_j, g_j, p_j and r_j are experimental fitting parameters.

(4) Autogenous volume strain

It has been widely accepted that autogenous volume strain $\varepsilon_g(t)$, which is caused by the hydration reaction of mortar matrix, is mainly related to the age of concrete and can be estimated by regression analysis from experimental data [44]:

$$\varepsilon_g(t) = g_0 + g_1 t + g_2 t^2 + g_3 t^3 + g_4 t^4 + g_5 t^5 \tag{14}$$

where g_0, g_1, g_2, g_3, g_4 and g_5 are experimental fitting parameters.

2.4. Numerical discretization

FEM is used in this paper to solve the continuous structure problem, and the discretized equations are presented in this Section. In order to study the thermo-mechanical coupling behavior of concrete, time-dependent thermal evolution should be studied first. The equilibrium equation of FEM for an unsteady-state heat transfer process is as follow [39]:

$$[J]\left\{\frac{\partial T}{\partial t}\right\} + [H]\{T\} = \{F\} \tag{15}$$

where $[J]$ is the heat capacity matrix, $[H]$ is the heat conductivity matrix and $\{F\}$ is the load heat vector under hydration and thermal convection.

Assuming that the spatial domain and the time domain are uncoupled, in a small time interval $\Delta t = t_i - t_{i-1}$, $\left\{\frac{\partial T}{\partial t}\right\}$ can be approximated by the backward finite difference:

$$\left\{\frac{\partial T}{\partial t}\right\} = \frac{1}{\Delta t}[\{T(t_i)\} - \{T(t_{i-1})\}] \tag{16}$$

Since the elastic modulus E and creep compliance C of the cement matrix are time-dependent, and the concrete specimen is elastic in the early age, the FE incremental method [1] (mid-point stiffness method) can be employed for the strain-stress analysis. The method decomposes the nonlinear problem into a series of piecewise linear problems. The constitutive equation within each time interval can be defined by the elastic modulus and creep compliance at the mid-point of the interval. The strain increment between time τ_i and τ_{i-1} is represented as:

$$\{\Delta\varepsilon_i\} = \{\Delta\varepsilon_i^e\} + \{\Delta\varepsilon_i^T\} + \{\Delta\varepsilon_i^c\} + \{\Delta\varepsilon_i^g\} \tag{17}$$

where $\{\Delta\varepsilon_i^e\}$, $\{\Delta\varepsilon_i^T\}$, $\{\Delta\varepsilon_i^C\}$ and $\{\Delta\varepsilon_i^g\}$ are elastic strain increment, temperature strain increment, creep strain increment and autogenous volume strain increment, respectively.

It is assumed that the stress rate, $\frac{d\sigma}{d\tau}$, of the interval, $\Delta\tau_i$, is constant, thus the increment of elastic strain $\{\Delta\varepsilon_i^e\}$ based on Eq. (7) is obtained as:

$$\{\Delta\varepsilon_i^e\}=\frac{1}{E(\tau_{i-0.5})}[Q]\{\Delta\sigma_i\} \tag{18}$$

where $E(\tau_{i-0.5})$ is the elastic modulus of concrete at the midpoint of interval $\tau_{i-0.5} = \frac{1}{2}(\tau_i + \tau_{i-1})$, and $[Q]$ is a sixth-order symmetric matrix considering the influence of Poisson's ratio for spatial problems [1].

According to the constitutive equations of creep expressed in Eq. (10), the creep strain increment $\{\Delta\varepsilon_i^C\}$ can be obtained from Eq. (19):

$$\{\Delta\varepsilon_i^C\} = \{\eta_i\} + q_i\{\Delta\sigma_i\} \tag{19}$$

where η_i and q_i are explicitly given by:

$$\eta_i = \sum_{j=1}^{m}(1 - e^{-r_j\Delta\tau_i})w_{ji}$$

$$q_i = C(\tau_i, \tau_{i-0.5})$$

where w_{ji} are defined incrementally as $w_{j1} = \Delta\sigma_0\phi_j(\tau_0)$ and for $i \geq 0$:

$$w_{ji} = w_{j,i-1}e^{-r_j\Delta\tau_{i-1}} + \Delta\sigma_{i-1}\phi_j(\tau_{i-1-0.5})e^{-0.5r_j\Delta\tau_{i-1}}$$

Considering Eqs. (17). (18) and (19), the relation between stress increment and strain increment is derived as:

$$\{\Delta\sigma_i\} = [\bar{D}_i](\{\Delta\varepsilon_i\} - \{\eta_i\} - \{\Delta\varepsilon_i^T\} - \{\Delta\varepsilon_i^g\}) \tag{20}$$

where

$$[\bar{D}_i] = \frac{E(\tau_{i-0.5})}{1 + q_iE(\tau_{i-0.5})}[Q]^{-1}$$

The overall equilibrium equation in interval $\Delta\tau_i$ is denoted as:

$$\int[B]^T\{\Delta\sigma_i\}dV = \{\Delta P_i\} \tag{21}$$

where $\{\Delta P_i\}$ is the total load increment.

By introducing Eq. (20) into Eq. (21), the stiffness equation of concrete accounting for creep and volume deformation under hydration heat is

$$[K_i]\{\Delta\sigma_i\} = \{\Delta P_i^T\} + \{\Delta P_i^C\} + \{\Delta P_i^g\} \tag{22}$$

where $[K_i]$ is the globe stiffness matrix at time τ_i, $\{\Delta P_i^T\}$, $\{\Delta P_i^C\}$ and $\{\Delta P_i^g\}$ are the load increment caused by temperature deformation, creep deformation and autogenous volume, respectively, and their expressions are shown as follows:

$$[K_i] = \int[B]^T[\bar{D}_i][B]dV \tag{23}$$
$$\{\Delta P_i^T\} = \int[B]^T[\bar{D}_i]\alpha_T\Delta T_i\,dV \tag{24}$$
$$\{\Delta P_i^C\} = \int[B]^T[\bar{D}_i]\{\eta_i\}dV \tag{25}$$
$$\{\Delta P_i^g\} = \int[B]^T[\bar{D}_i]\{\Delta\varepsilon_i^g\}dV \tag{26}$$

3. The simulation approach

3.1. The Diffuse meshing method

Different to the indirect meshing method for mesoscopic model, by which individual material components are not required to be explicitly modelled, the diffuse meshing method [45] is developed on the basis of the mapping meshing method, by which heterogeneous material properties are directly projected on the Gauss points of regular finite element grid. As a result, the diffuse meshing method can model multiple material components in one finite element, thus is capable of allocating different attributes to different nodes of a finite element as shown in the 2D mesh of Fig.4. The elements across the material interface are all regular four-node quadrilateral elements for an aggregate material in mapped meshing. By the different attributes at the Gaussian point at the two sides of the aggregate boundary, the diffuse meshing method can approximately present the topology of complex aggregate boundaries and subsequently simulate the material discontinuity across the aggregate and cement matrix interface.

After establishing the mesoscopic model in Section 2.1, the next step is to identify whether a Gaussian point is of cement or aggregate across the entire meshed domain. This can be conveniently done as the complex shape of all aggregates in this paper are reconstructed by using the implicit T-spline algorithm, so whether a Gauss point is located within an aggregate or the cement matrix can be determined using their respective T-spline functions. For example, considering a set of implicit T-spline functions $\{f_i(r, s, t) = 0\}_{i=1}^{n}$ of the aggregates (n is the number of aggregates), the values of the functions at each Gauss point (x_g, y_g, z_g) is computed as $\{f_i(x_g, y_g, z_g)\}_{i=1}^{n}$. If their values are all greater than zero, it means that this Gauss point is not located within any of the aggregates, thus defined as cement point. Otherwise it must be within one of the aggregates as specified by its co-ordinates. Using this mesoscopic model, the associate mechanical properties can be assigned to the Gauss points within aggregates and cement mortar material, respectively, for modeling their individual behavior and representing the heterogeneity of concrete.
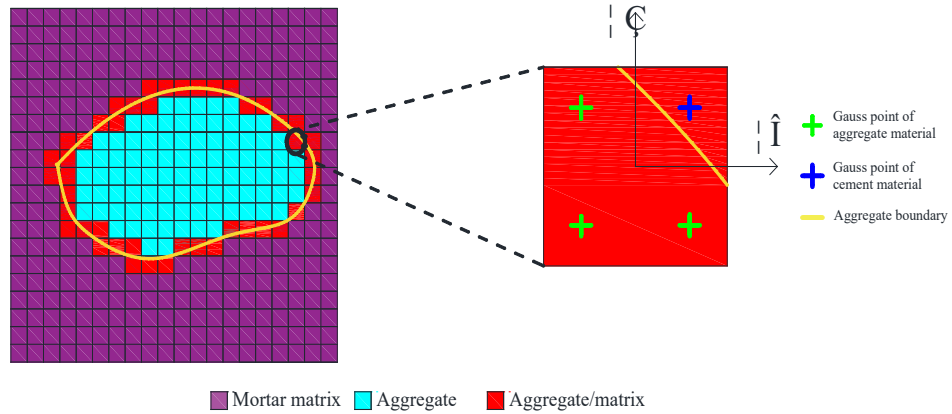

Fig.4. Local material distribution by using the diffuse meshing method

Compared to the conventional FEM, the main feature of the diffuse meshing method is the stiffness matrix $[k]$ of each finite element that is calculated as a function of the distribution of different material components:

$$[k] = \sum_{i=1}^{N} w_i B(\xi_i, \eta_i, \zeta_i) D(\xi_i, \eta_i, \zeta_i) B(\xi_i, \eta_i, \zeta_i) \tag{27}$$

where N is the number of Gauss points, w_i is the weight associated with each Gauss point, ξ_i, η_i and ζ_i are the coordinates of Gauss Points i, B is the shape function matrix and D is the stiffness matrix of the material at Gauss point i.

In our case, the diffuse meshing method is combined with the solution of FEM for the linear viscoelasticity problem, as shown in Eq. (22), which requires further modification of the equivalent node load increment $\{\Delta P_i\}^e$. Thus, the temperature load increment $\{\Delta P_i^T\}^e$ should incorporate the corresponding material coefficient of thermal expansion α_T of each Gauss point. Since creep or shrinkage in the aggregates is negligibly small, it is assumed that the creep load increment $\{\Delta P_i^C\}^e$ and the autogenous volume load increment $\{\Delta P_i^g\}^e$ at the Gauss points of the

aggregate material are equal to zero. Hence, they are calculated, respectively, as:

$$\{\Delta P_i^T\}^e = \sum_{i=1}^{N} w_i \alpha_T B(\xi_i, \eta_i, \zeta_i) D(\xi_i, \eta_i, \zeta_i) \Delta T_i \tag{28}$$

$$\{\Delta P_i^C\}^e = \sum_{i=1}^{N} w_i \alpha_T B(\xi_i, \eta_i, \zeta_i) D(\xi_i, \eta_i, \zeta_i) \{\eta_i\} \Delta T_i \tag{29}$$

$$\{\Delta P_i^g\}^e = \sum_{i=1}^{N} w_i \alpha_T B(\xi_i, \eta_i, \zeta_i) D(\xi_i, \eta_i, \zeta_i) \{\Delta \varepsilon_i^g\} \Delta T_i \tag{30}$$

The model developed using the diffuse meshing method can be used to discretize multi-phase materials using regular elements without the need to follow the material interfaces, such as the aggregate/matrix interface in this paper. Since different material properties are assigned to the Gaussian points on the different sides of the interface, the interfacial properties are 'diffused' linearly between the two closest sets of the integration points across the interface, representing a simplified form of the ITZ. Unlike the exact meshing method, by which the meshing has to follow the material interfaces, the diffuse meshing method allows an easy generation of regular grid and requires significantly less pre-processing and computational time, especially for models with complex aggregate geometry. It is worthy of noting that when the diffuse meshing method is used, the size of the elements across material interfaces is an important factor to not only the overall accuracy of the FE model, but also the simplification of the interface, as the width of the 'diffused' zone depends on the distance between the two closest sets of the cross-interface Gaussian points. Therefore, a grid-scale convergence analysis of the diffuse meshing method is carried out. For simplicity, the single aggregate concrete model (Fig.5) is analyzed by the diffused meshing method and compared with the results of the full three-phase model (exact meshing). The model is divided into a regular grid composed of eight-node hexahedral elements. Five different element sizes, i.e., 2mm (Mesh 1), 2.5mm (Mesh 2), 4mm (Mesh 3), 5mm (Mesh 4) and 10mm (Mesh 5), are respectively, considered. Fig.6 shows the cross-sections of the two meshing schemes. The reference model (Fig.6a) is a three-phase model using exact meshing method, where it is assumed that the interface thickness is 1/100 of the diameter of aggregate, and the elastic modulus is 75% of the mortar, as recommended by other researchers [46].
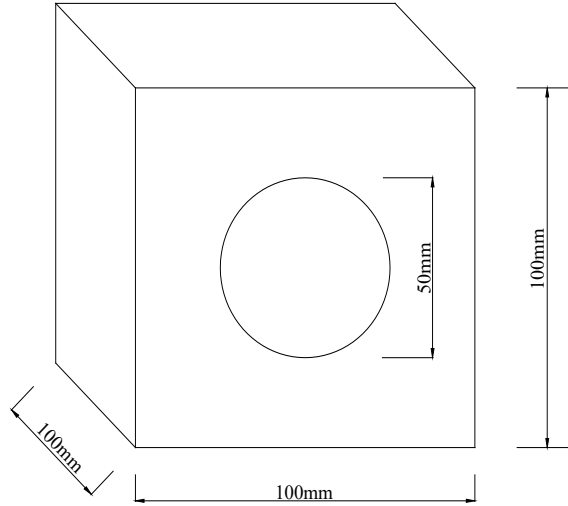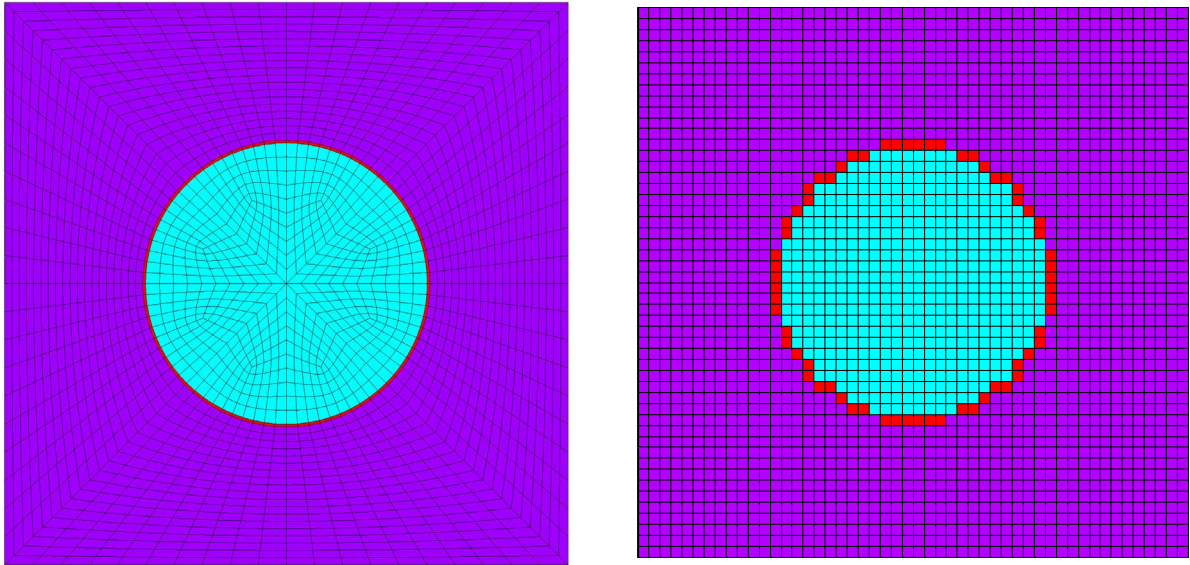

Fig.5. The single aggregate concrete model

(a) the three-phase model with the exact meshing   (b) the present model with the diffuse meshing

Fig.6. The cut-off grid discretization

Fig.7 shows the stress-displacement curves in different grid scales when the model is subjected to a vertical displacement from the top. It can be found that the simulation results have converged well as the size of the elements decreases and are very close, if not identical, to the results of the full 3-phase model when the size of the diffuse elements is 2mm, which is equal to one fifth of the diameter of the minimum aggregate(10mm). Similar observations were also found by N'Guyen [45] and Grondin [47]. The satisfactory comparison suggests that although the interface is not considered independently in the present model, the diffusion of material properties between the Gaussian points is capable of dealing with material discontinuity across the aggregate/matrix interfaces without having to separate them before meshing. Evidently, this will significantly reduce the complexity and workload of meshing and the subsequent simulation, which is less obvious for the model in Fig.7 as the aggregate is only a sphere while will be much more prominent when the aggregate is a more realistic one. In addition, the above success in introducing the diffuse meshing method to simulate materials discontinuity can be extended further to include detailed ITZ properties in the model, though additional research is required to find the best approach to make sure sufficient Gaussian points be located within a ITZ by, e.g., using second-order or higher-order Gaussian difference.
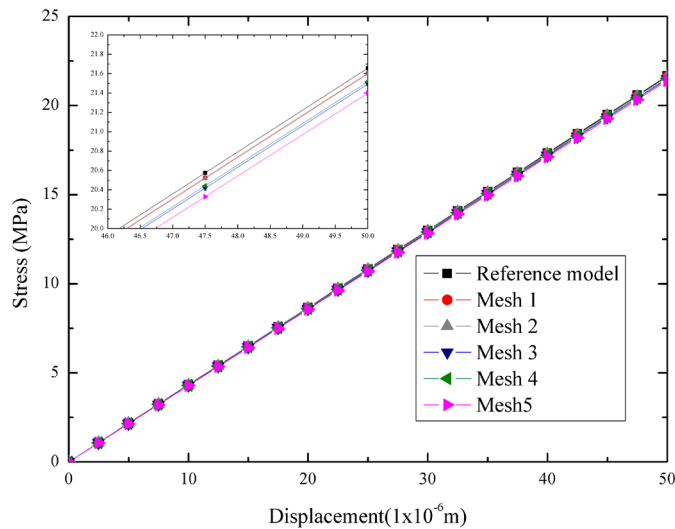

1

Fig.7. The stress development in different grid scales

3.2. Model parameters

It is assumed that both the aggregate and cement matrix are isotropic with their own thermal-mechanical parameters. The time-independent input parameters summarized in Table 1 are from experiments and can be found from the literature [1, 48, 49]. The Poisson's ratios of the materials are assumed to remain constant during the whole hydration process.

For a thermo-mechanical analysis, the time-dependent parameters at mesoscale level, including adiabatic temperature rise, creep and autogenous volume deformation, are also required, but very often are not available due to the absence of appropriate test data. There are some empirical formulas of these parameters obtained through concrete homogenization and calibration of global performance of a material specified by , e.g., Eq. (4), Eq. (8), Eq. (11) and Eq. (14). Table 2 shows the time-dependent parameters based on the experimental results by Fu [42], which will be used in simulating homogeneous concrete. The meso-parameters required for the meso-model are evaluated from homogeneous concrete macro-model by the following the calibration process in Section 4.

Table 1 The time-independent parameters for the cement matrix and the aggregates

Constituents	Elastic modulus (GPa)	Poisson's ratio	CLTE (℃$^{-1}$)	Density (kg m^{-3})	Specific heat (kJ kg^{-1} ℃$^{-1}$)	Thermal conductivity (kJ m^{-1} h^{-1} ℃$^{-1}$)
Cement	20	0.2	1.6×10^{-5}	2273	1.158	8.125
Aggregates	40	0.2	0.55×10^{-5}	2680	0.716	10.504

Table 2 The functions for the time-dependent parameters

Parameters	Functions (t, τ:d)
Adiabatic temperature rise	$\theta(\tau) = 30/(3.57 + \tau)$
Elastic modulus	$E(\tau) = E_0\tau/(4.5 + \tau)$
creep compliance of concrete	$C(t,\tau) = (2 + 75\tau^{-0.48})\left(1 - e^{-0.4(t-\tau)}\right) + (3 + 20\tau^{-2.5})$ $\left(1 - e^{-0.04(t-\tau)}\right) + 28\tau^{-0.02}\left(1 - e^{-0.02(t-\tau)}\right)$
The autogenous volume strain of concrete	$\varepsilon(\tau) = 2.3954 - 0.678\tau + 0.00569\tau^2 - 1.93 \times 10^{-5}\tau^3 +$ $2.87 \times 10^{-8}\tau^4 - 1.58 \times 10^{-11}\tau^5$

3.3. Simulation procedure

Based on the diffuse meshing approach described in Section 3.2, a computer program called COCE3D-DM is developed from an existing FEM program CORE3D that is a rheological analysis software based on elasto-viscoplastic constitutive relation [50, 51]. The simulation procedure to calculate early-age restrain stress for the present model is as follows:

(1) Calculation of temperature field

The thermal analysis was performed on ANSYS using the mapped meshing method due to the rapid thermal movement in the laboratory-sized concrete, which showed a small nodal temperature difference between material components in one finite element. APDL (ANSYS Parametric Design Language) in ANSYS was used   to define the boundary conditions and the hydration function of mortar.

(2) Calculation of stress field under temperature, creep and autogenous volume deformation

a. The nodal temperature increments of one day intervals are obtained from the dynamic temperature field analysis in (1).

b. Taking the temperature, creep compliance and autogenous volume deformation increments as the input data, the stress-strain realtion of the present model is calculated by using COCE3D-DM at time step of 1d, for a total

period of 28d (whole curing time period of concrete).

c. Creep is a strain that increases continuously within the time period, which is caused mainly by the combined action of temperature and autogenous volume deformation. In this paper, the creep is calculated as the superposition of the creep generated from each of the previous days and that of the current day, as the concrete is assumed to be linearly elastic in the early age. Assuming that the stress field of the current day (day m) generated from day i (i=1,2,3…m) is from Step i_m , the total stress field under temperature, creep and autogenous volume deformation on the m-th day is the sum of the creep calculated from Step 1_m, Step 2_m..., Step m-1_m and Step m_m , where Step m_m is the step to calculate the creep from the action of the temperature and autogenous volume deformation of current day, i.e., day m.

4. Meso-parameter calibration

The proposed thermo-mechanical meso-model is further studied in this section. The cross-scale (macro- and micro-) numerical simulations in this section serve two purposes, namely verifying the reliability of the proposed diffuse meshing method applying in the thermo-mechanical analysis, and calibrating the relevant time-dependent meso-parameters mentioned in Section 3.2 for cementitious material in the mesoscopic model. The FE results of the homogeneous concrete model and the results of the mesoscopic model using the diffuse meshing method are compared to calibrate the meso-parameters, so that both models can produce comparable macro scale performance. After the validation and calibration, the proposed model is employed to study the evolution mechanism of self-restraint stress from the mesoscale level. Figure 8 shows the homogeneous and isotropic concrete model (Fig.8a)and the new model with heterogeneous meso-structure. The size of models is 150 mm × 150 mm × 150 mm, and the element size of the model is 7.5mm and 2mm respectively.

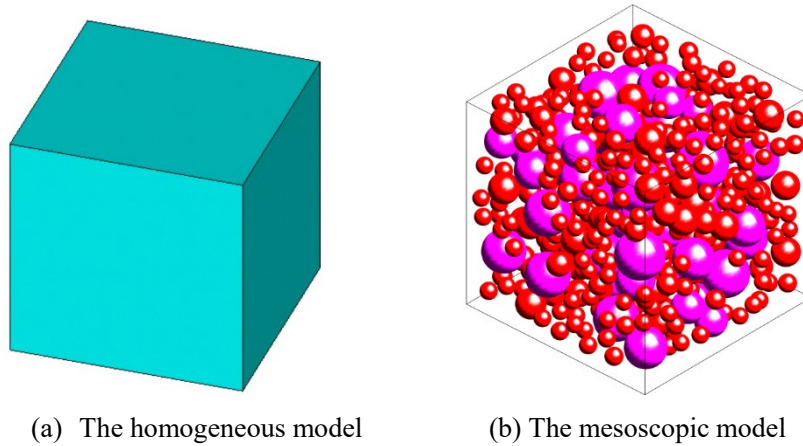(a) The homogeneous model   (b) The mesoscopic model

Fig.8. Different models of concrete sample

4.1 Validation of adiabatic temperature rise

Typical thermal parameters of concrete are normally estimated using the following homogenization process.

$$\rho_c = \sum p_i \rho_i \tag{31}$$

$$\lambda_c = \sum p_i \lambda_i \tag{32}$$

$$c_c = \sum k p_i c_i \tag{33}$$

where ρ_c, λ_c and c_c are the density, heat conduction coefficient and specific heat of concrete respectively, as

shown, e.g. in Table 1. p_i, ρ_i, λ_i and c_i are, respectively, mass ratio, density, heat conduction coefficient and specific heat of component i (aggregate or cement mortar). k is the correction coefficient for estimating specific heat capacity, which is generally taken as 1.05. The aggregate volume content of the present model is 28.67%. The equivalent material parameters of the homogeneous concrete model are determined as shown in Table 3.

Table 3 The equivalent thermal parameters for the homogeneous model

Material	Density (kg m^{-3})	Specific heat (kJ kg^{-1} °C^{-1})	Thermal conductivity (kJ m^{-1} h^{-1} °C^{-1})
Concrete	2389.68	1.067	8.890

In addition, the hydration heat of cement material, which is the main heat generation source of concrete under the adiabatic condition, also need to be characterized. However, the thermal analysis in practical engineering usually employs adiabatic temperature rise θ of concrete material (Table 2). In the absence of measurement data, the hydration heat of cement Q_{cement} can be estimated by the following formula:

$$Q_{cement} = \frac{\theta c_c \rho_c}{w_{cement}} \tag{34}$$

where w_{cement} is the content of cement in concrete.

The numerical simulations of adiabatic temperature rise are conducted subjected an initial temperature of 20℃ and no heat exchange with the surrounding environment (adiabatic condition). The homogeneous model uses the parameters given in Table 2 and Table 3, while the mesoscopic model uses the parameters provided in Table 1 and the calculated from Eq. (34). The time interval is set to 0.2d, small enough to capture the heat generated at the very early age. As shown in Fig.9, the average temperatures of both models are in good agreement with the theoretical solution shown in Table 2. The comparison also demonstrates that a model with homogenous concrete properties calculated from the individual properties of the material components can predict global responses of the concrete that agree well with the predictions from the mapped element model where material properties of the individual components are used independently in the calculation. This observation forms the basis on which the time-dependent parameters of material components, such as cement and aggregate, are evaluated reversely through comparisons between the homogenous concrete model and the meso mapped meshing model.
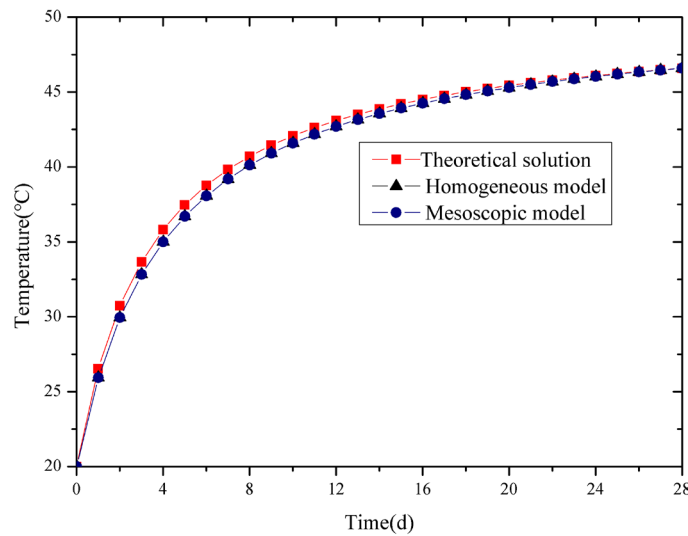

Fig.9. Temperature development of concrete under the adiabatic condition

4.2 Validation for creep

The aim of this section is to determine the creep parameters of cementitious material in the mesoscopic model,

and to verify the creep simulation by applying the diffuse meshing method. The boundary conditions are defined as follows. The bottom surface of the model is fixed vertically in all directions. For the creep test, the top surface of the model is subjected to a sustained axial compressive stress of 10MPa. The elastic modulus of the homogeneous concrete model is 24.7GPa calculated from the equivalent elastic modulus of the mesoscopic model at the elastic stage, and the creep compliance of the concrete model is given in Table 2.

The creep compliance of cement mortar can be approximately evaluated based on the compliance of the concrete. The creep of concrete in early age is mainly produced by cementitious material while the presence of aggregates may only limit the deformation, which is therefore considered to be dependent on the content of cement mortar [52]. Some studies [53, 54] found that there is an approximately linear relationship between the creep of concrete and the content of cement mortar. Neville [55] proposed that the creep compliance between concrete c^c and cement mortar c^m satisfy the following relation,

$$\lg \frac{c^c}{c^m} = a \lg \frac{1}{\left(1 - f_a - u\right)}$$ (35)

where a is an experimental constant; f_a and u are, respectively, the content of aggregate and un-hydrated cement.

Eq. (35) can be simplified [15] by incorporating the influence of un-hydrated cement content into the experimental constant a, thus

$$c^m = c^c / \left(1 - f_a\right)^a$$ (36)

FEM is used to calculate the homogeneous concrete model using the creep compliance in Table 2. The diffuse meshing method is used in the mesoscopic model with the creep compliance of cement defined by Eq.(36), where a is a factor to be determined. Taking the result of mesoscopic model as the reference result, by changing the value of a, comparisons are made between the creep compliance of the concrete and the diffuse meshing models to search for an a that gives an equal creep compliance from both models. Fig.10 shows the searching process, where an value of 1.8 for the diffuse meshing model results in a creep curve that is very close to the one from the concrete model. Thus the creep compliance of the cement can be calculated by Eq.(36) when a is 1.8, then the creep response of the mesoscopic model is then reanalyzed using 1.8
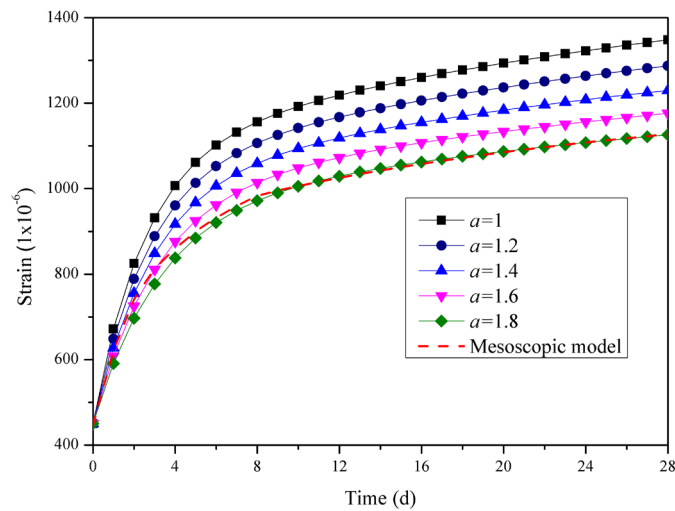

Fig.10. Strain evolutions in creep analysis under different experimental constant

When the concrete is subjected to sustained stress $\sigma(\tau_0)$ at age τ_0, the total strain at time t is the sum of instantaneous elastic strain and creep strain, the theoretical predictions for concrete creep is derived from Eq. (7) and Eq. (10):

$$\varepsilon(t) = \varepsilon_e(t) + \varepsilon_C(t) = \frac{\sigma(\tau_0)}{E(\tau_0)} + \sigma(\tau_0)C(t, \tau_0) = \sigma(\tau_0)J(t, \tau_0) \tag{37}$$

where $J(t, \tau_0) = 1/E(\tau_0) + C(t + \tau_0)$ is creep function.

The theoretical solution is obtained by incorporating the creep compliance in Table 2 into Eq. (37). Fig.11 compares the strain evolutions calculated numerically and analytically. Under the constant stress, the numerical results of the diffuse meshing model using Eq.(36) and the above calibrated a, and the homogeneous concrete model using FEM are in good agreement with the theoretical solution, which validate the capability of the proposed mesoscopic model and corresponding calibration process of the meso parameters.
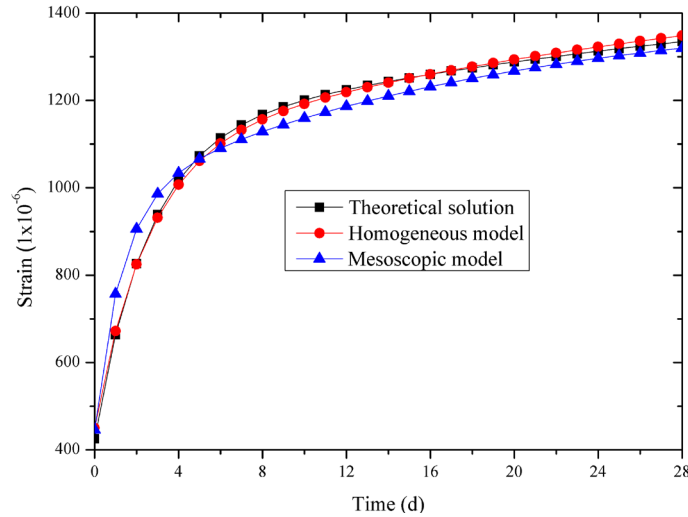
Fig.11. Comparison between the theoretical solution and numerical results for creep analysis

4.3 Validation for autogenous volume deformation

This section evaluates the autogenous volume deformation parameters for cement materials and verify the use of the diffuse meshing method in simulating autogenous volume deformation. The average strain of the homogeneous model is calculated by the FEM using the autogenous volume strain function given in Table 2. The autogenous volume deformation of cement materials is assumed to be approximately related to the amount of cement in a forma similar to Eq.(36), i.e., $\varepsilon_g^m = \varepsilon_g^c / (1 - f_a)^{a_g}$. The diffuse meshing method is carried out to simulate the mesoscopic model and similar comparisons are made with the solutions from the concrete model to determine the constant a_g by following the procedure in the creep analysis. The results are shown in Fig.12, from which a satisfactory comparison is observed when a_g is 1.3.
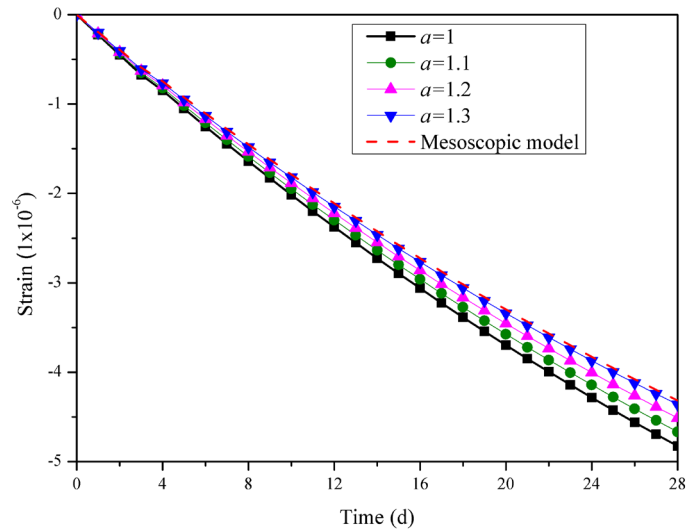
Fig.12. Strain evolutions in autogenous volume deformation analysis under different experimental constant

For the homogenously isotropic concrete model, the theoretical solution of average strain is equal to one third of the autogenous volume strain $\varepsilon_g(t)$ that is given in Table 2. Fig.13 shows the average strain evolutions under the autogenous volume deformation. It can be found that by using the calibrated autogenous volume deformation of cement, the results of the diffuse meshing model are in good agreement with the theoretical solution and the solution from the concrete model.
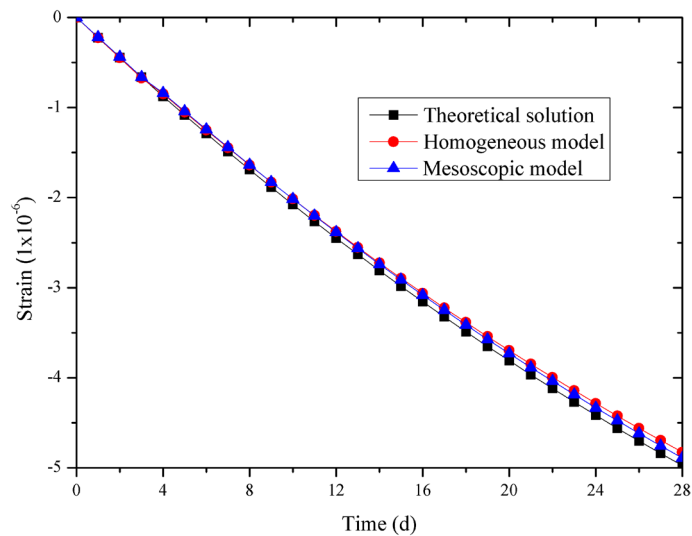
Fig.13. Comparison between the theoretical solution and numerical results for autogenous volume deformation analysis

5. Numerical results and analysis

Based on the parameters given in Table.1 and the calibrated ones in Section 4, the temperature and stress fields in the hydration process of the concrete are obtained by applying the proposed diffuse meshing meso-model. The evolution mechanism of self-restrain stresses is studied, and the impact of simplified aggregate mesostructure on the thermo-mechanical behavior is studied in this section.

5.1. Comparisons of temperature field

During the thermal analysis of all the concrete meso-models, it is assumed that both the initial (cast) temperature and the ambient temperature are constantly at 20℃. Unlike the analysis of adiabatic temperature rise, the surface of the concrete block exchanges heat with the environment, and the corresponding convection coefficient β is set to 18.4kJ m^{-1} h^{-2} ℃$^{-1}$, reproducing an almost stagnant air condition [1]. Fig.14 shows the schematic diagram of the model for thermal simulation, where Point O is the center of the concrete.
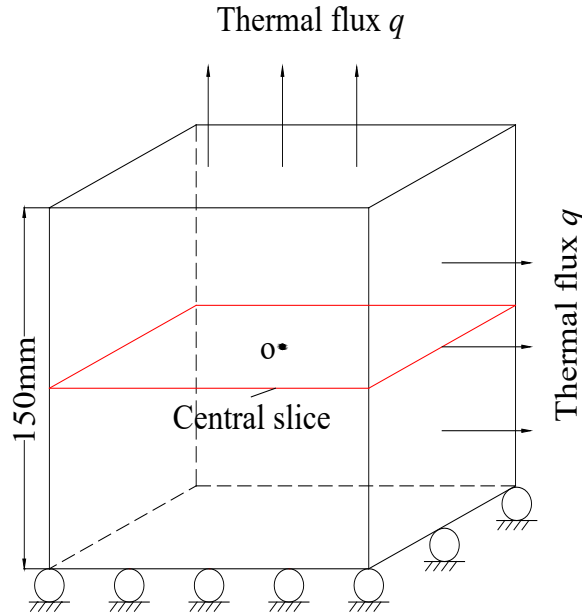
Fig.14. The schematic diagram of the calculated model

The temperature histories at the center point of the five models shown in Fig.2 are plotted in Fig.15, which are all consistent with the evolutionary law. Initially, there is a rapid increase in the temperature because the rate of hydration heat is greater than the heat loss transferred to the external environment, and the maximum temperature rise from the initial value is about 1.2℃ at 0.6d. With the decrease of hydration heat, the heat loss becomes the dominant factor, which leads to a progressive reduction in the internal temperature to the environmental temperature of 20℃ (external temperature). The temperature evolution of all the models follows a similar trend, which is in consistent with the numerical result of Xu [15] and Lee [56].
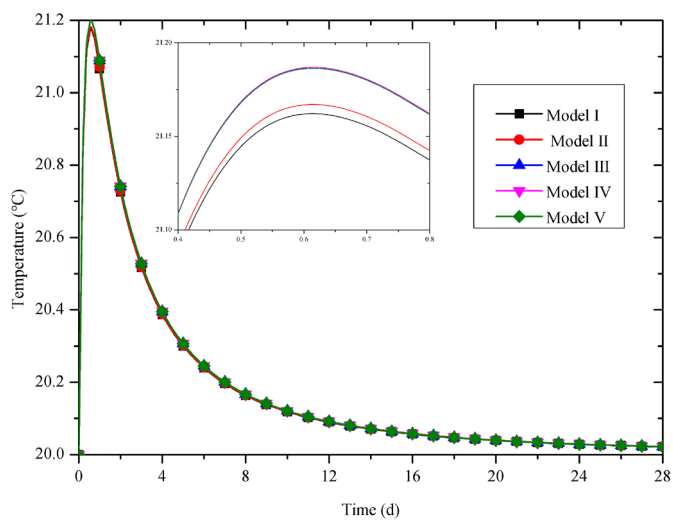

Fig.15. Comparison of temperature development at midpoint of each model

Fig.16 shows the temperature distribution of the five models at the central section at 1.0 day. Due to the heat

exchange between the surface and the air, the temperature of the surface layer is relatively lower than the center temperature, thus forming a temperature gradient within the concrete that is approximately concentric due to symmetry. The spatial temperature distributions of the five models are similar, and there are only small differences in temperature and gradient, though the temperature gradient is generally very small since size of the specimens is small.

There are slightly more elements of mortar material in the crushed aggregate model (Model II~ Model V) than in the simplified spherical aggregate model (Model I). Hence a small difference (0.12%) of peak temperature can be observed from Fig.15. In fact, the hydration process of the concrete samples involves heat generation and heat loss, which are, respectively, associated with the content of cement mortar and the convection coefficient.
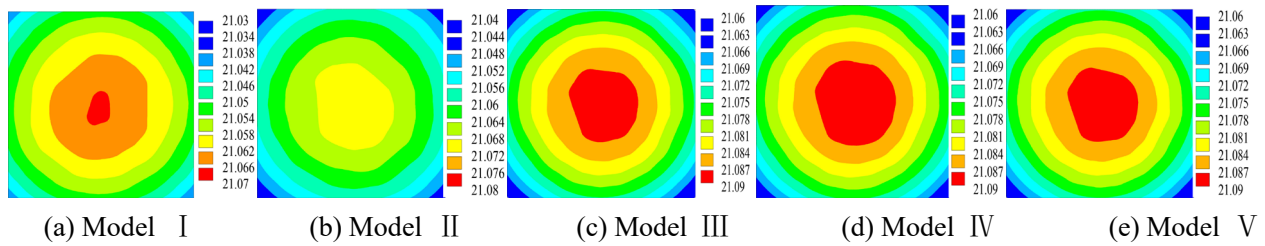

| (a) Model Ⅰ | (b) Model Ⅱ | (c) Model Ⅲ | (d) Model Ⅳ | (e) Model Ⅴ |

Fig.16. Temperature distribution in horizontal central slice view of models at 1.0 d

5.2. Results of the spherical aggregate model

Generally, temperature gradients in the time and space domains will produce temperature deformation and temperature stress in early-age concrete. If the material properties of each component are independent with age, the temperature stress in the interior of concrete is self-balanced in the hydration process without external load and restraint [1], which means that the temperature-dependent compressive stress emerged in the temperature rising process will be progressively offset by the tensile stress produced by the cooling. However, the elastic modulus of cementitious material apparently increases due to the continuous hardening of young concrete. Therefore, for the entire temperature history, varying from the casting temperature to the peak value and then falling back to the ambient temperature (equal to casting temperature in this paper), the compressive stress induced during heating will be less than the tensile stress induced during cooling. Along with the creep and autogenous volume shrinkage deformation, nonnegligible residual tensile stress termed as self-restraint stress will be produced in the concrete at the end of the thermal cycle.

For Model I (simplified spherical aggregate model), the temperature load is obtained according to the results in Section 5.1, and the creep and autogenous volume deformation are estimated based on the calibration in Sections 4.2 and 4.3. The stress-strain analysis is carried out by using COCE3D-DM. Fig.17 (a) and Fig.17 (b) show, respectively, the major principal stress contours of the center section of Model I at 1d and 28d. Obvious stress inhomogeneity in the concrete sample is observed, indicating that the mesoscopic models can predict a more realistic stress filed than that produced by the homogenous concrete model. From the figures, the distribution characteristics of major principal stresses in the concrete are as follows:

(1) As the volume expansion of cement mortar is constrained by the aggregates, the major principal stress in the cement mortar is mainly compressive whereas in the aggregates it exhibits tensile during heating (1d), as shown in Fig.17 (a);

(2) When the thermal equilibrium of heat exchange with the environment is reached, the stresses in the cement mortar and the aggregates (Fig.17 (b)) are opposite to those at 1d.

(3) Due to the thermo-mechanical mismatch, significant self-restraint effect is produced in the vicinity of the interfaces between the aggregate and cement mortar, resulting in mismatched strains and considerably higher stresses near the interfaces.
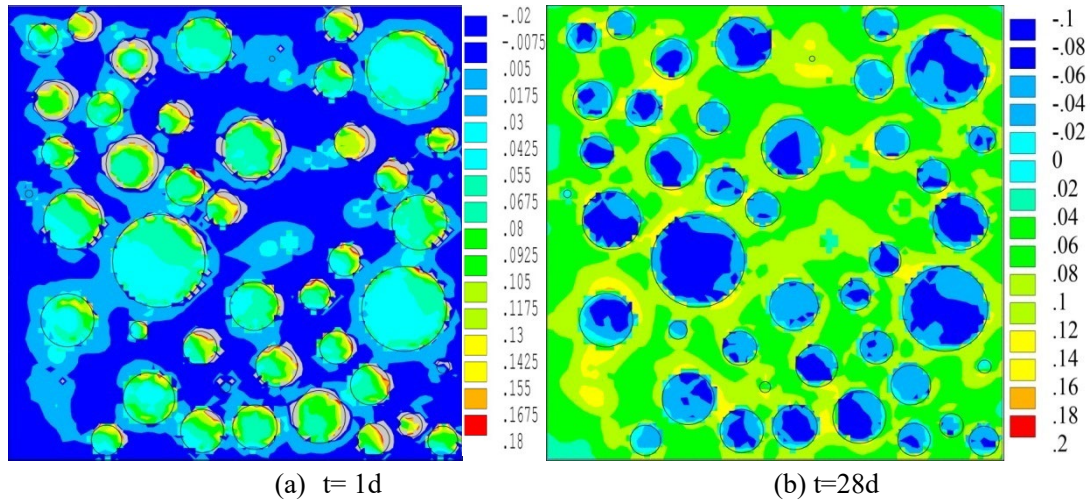
<div align="center">(a) t= 1d   (b) t=28d</div>

<div align="center">Fig.17. Major principal stress contours on center slice in Model I, MPa</div>

Similar observations can also be found in the numerical simulations by Xu [15]. Although interface is not fully represented in this mesoscopic model, the proposed matrix/aggregate elements have reasonably simulated the stress concentration at the aggregate/matrix "interface" where the stiffness mismatches between aggregate and cement are duly reflected by the proposed diffuse meshing element.

The tensile strength of aggregate is much higher than that of cement mortar, and therefore it is generally considered that the failure of concrete is caused by the generation and expansion of micro cracks which mainly arise in the interior of cement mortar or the interface. Assuming that the damage of aggregate does not occur, only the evolution of major principal stress in cement mortar material is discussed in this work. The present model of concrete accounts for multiple factors, i.e., temperature, creep and autogenous volume deformation in the early age. In order to investigate the influence of these factors on the stress evolution of the concrete, the results under the factors of temperature, creep and autogenous volume deformation can be evaluated separately since the concrete is assumed linearly elastic throughout the simulation process. That is to say, the total stress response under the multiple factors is the linear superposition of those from the independent factors.

The maximum major principal stress considering the combined factors and the individual independent factors are depicted in Fig.18. It can be observed that the maximum major principal stress is tensile in the curing process and the stress evolution displays different patterns under different factors, as discussed below:

(1) Considering the temperature factor, the stress increases rapidly with the rapidly rising of temperature, reaching the peak value at the end of 1d. The maximum principal stress then decreases to the lowest at the end of 4d and finally tends to be stable under cooling. The maximum principal stress changes in consistence with the temperature variation (Fig.15).

(2) Under the autogenous volume deformation, the maximum principal stress increases continuously from concrete casting. The reason for this is that the volume of cement mortar shrinks due to the gradual hardening of concrete, and with the constrain of the embedded aggregates, the cement mortar is under tension all the time and this effect is gradually accumulating.

(3) The trend of evolution of the maximum principal stress in the concrete over the time under creep is similar to that of the concrete considering all multiple factors, and the magnitude of stress is approximately one-tenth of the latter.

In summary, the mechanical behavior of the concrete is governed primarily by temperature deformation during the first 4d. The effect of volume autogenous deformation is then more critical. After curing is completed, a residual tensile stress about 0.238MPa is generated inside the concrete under a temperature gradient of 1.2℃. Note that the

temperature gradient for large-volume concrete structures is much greater than the laboratory-sized concrete sample due to the larger content of cement, indicating the self-restrain stress of early-age concrete should not be ignored in practical design.
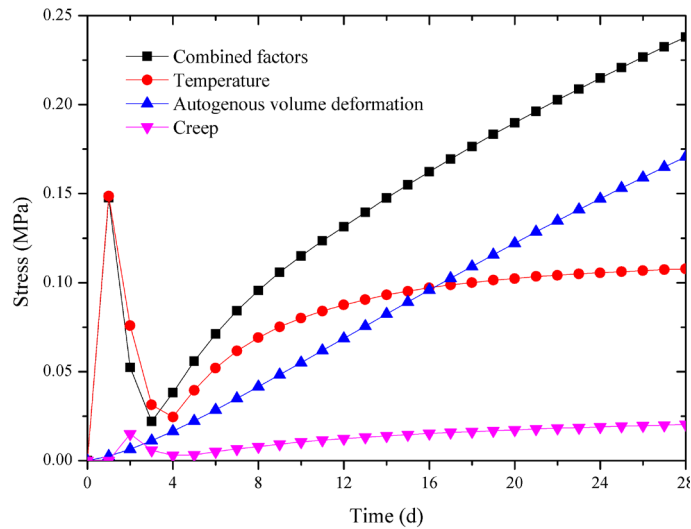

Fig.18. Maximum major principal stress evolution under different factor

5.3. The effect of aggregate morphology on mechanical behavior

In order to assess the effect of aggregates morphology on the mechanical behavior of the concrete, Model II is simulated by COCE3D-DM. Fig.19(a) and Fig.19(b) present the major principal stress contours at the center section of Model II at 1d and 28d, respectively. Compared with the results of Model I (Fig.17), the stress distributions of the two models are similar, both of which are in compression in the cement mortar during heating and in tension during cooling. Obvious stress concentration arises in the area where aggregates are very close. However, for Model II, when the cement mortar volume expands in the initial heating process, the embedded aggregates have no volume deformation, causing the cement mortar to "squeeze" the aggregates. Since the shape of the aggregate in Model II is angular, the distance between aggregates is shortened and the restraint effect of aggregate on cement mortar is more remarkable, thus stress concentration at the sharp edges of aggregate becomes more prominent. Meanwhile, the surface area of the crushed aggregate is larger than that of the simplified spherical aggregate, which increases the number of properties mismatch aggregate/matrix elements ("interface"), so that a larger area of stress concentration is predicted. The results have shown that, the morphology of the aggregates has a significant effect on the internal stress distribution of the concrete during temperature rising. When the volume of the cement shrinks in the process of temperature dropping, aggregate and cement mortar are in a relatively "separation" state, thus the restraining effect of aggregate is reduced, and the influence of the shape of aggregate on the mechanical behavior is relatively weakened.

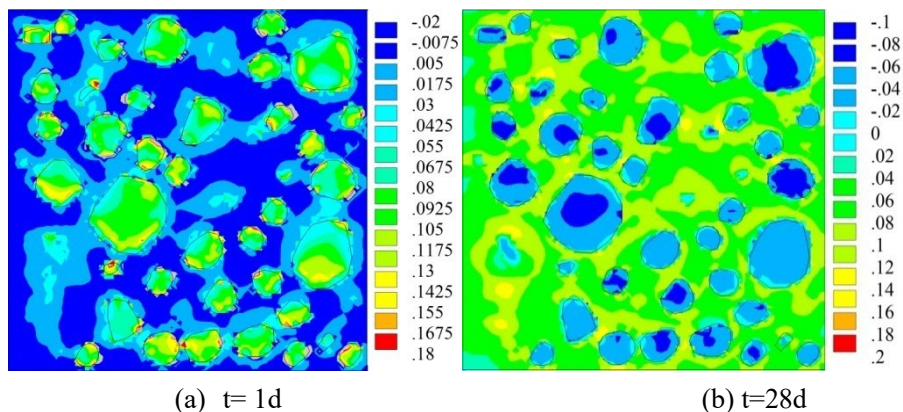(a) t= 1d   (b) t=28d

2

Fig.19. Major principal stress contours on center slice in Model II, MPa

Comparing the maximum major principal stress in the cement mortar of the two models with different aggregate shapes (Fig.20), the trends of stress with age are almost the same. However, there is a certain gap between the two models in terms of magnitude: the stress of Model II is about 6.5% larger than that of Model I in the initial stage of curing. After the later stabilization, the stress difference between the two models is less than 2.2%. It confirm that the morphology of aggregates has a more important impact in the processing of heating. Compared with the observations from Section 5.1, it can be concluded that the influence of aggregate morphology on the macro-mechanical properties of concrete (6.5%) is much greater than its influence on the thermal properties (0.12%), which should not be overlooked in the evaluation of self-restraint stress.
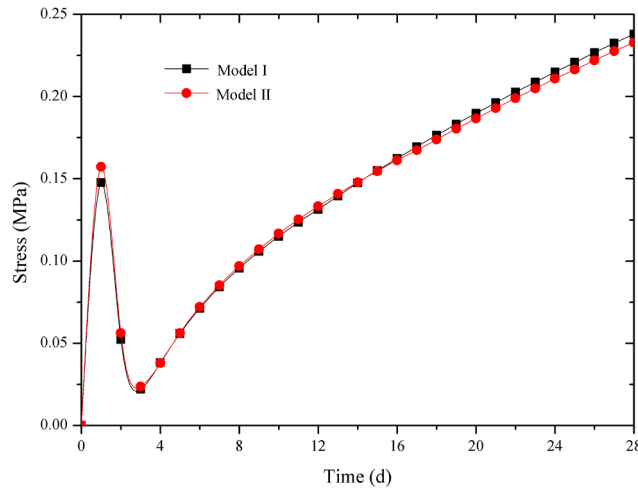

Fig.20. The maximum principal stress envelopes in different mesoscopic models

To understand further the influence of aggregate morphology on the local mechanical behavior of concrete, aggregate a is selected to analyze the. The midpoints between aggregate a and its seven surrounding aggregates, as shown in Fig.21, are selected as feature points (P1~P7) for the stress evaluation.
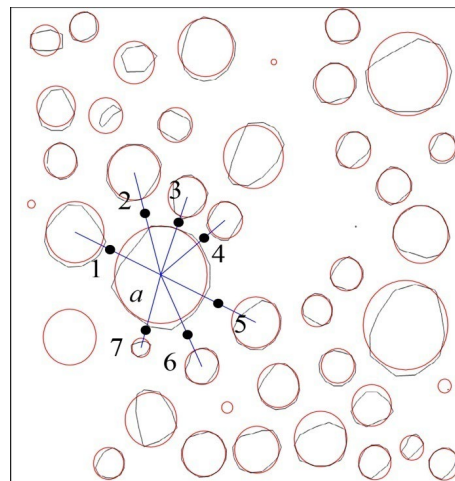

Fig.21. The feature points distribution on the central slice (the boundaries of spherical aggregates and crushed aggregates are marked in red and black, respectively)

Under the combined action of temperature, creep and autogenous volume deformation, Fig.22 shows that the major principle stress distribution in Model I is more uniform than in Model II, and this becomes more obvious with the increase of age. Comparing the stresses at the feature points, it can be found that when a feature point is closer

to an aggregate of a relatively large particle size or located in an area with compact aggregate distribution, the stress is greater, especially for Model II. In the case of considering temperature only, Fig.23 shows the thermal stress varies rapidly in the first four days due to the rapid thermal movement in the concrete. As the temperature gradient of the concrete slows down with the age, the accumulated stress gradually increases and stabilizes. In addition, the stress at feature point P1 in Model I is the largest in the heating period, while feature point P3, which is located near the sharp edge of the crushed aggregate, has the largest stress. In the simulation of autogenous volume deformation (Fig.24), the major principal stresses of feature points P1 and P4 in Model II at the end of curing at are 50.03% and 29.88% higher, respectively, than that of in Model I. This may be due to the fact that feature points P1 and P4 are both located with the properties mismatch element of Model II. The influence of aggregate morphology on creep is not discussed in this work, as the resulting stresses are much smaller..

It is worth noting that the only difference in the calculation of thermal and autogenous volume deformation stresses is the use of the equivalent nodal loads, as the meso scale global stiffness matrices are the same for both loading conditions. Since the linear expansion coefficients of aggregate (0.55×10^{-5}) and cement mortar (1.6×10^{-5}) have the same order of magnitude, the discrepancy of the temperature nodal loads at each Gauss point in the cement-aggregate element is much smaller than the nodal loads of autogenous volume deformation, where the deformation of aggregates is assumed to be zero. Therefore, the stress evolution of these points in the properties mismatch element for the autogenous volume deformation simulation shows more obvious difference than the simulation of temperature by using the diffuse meshing method.
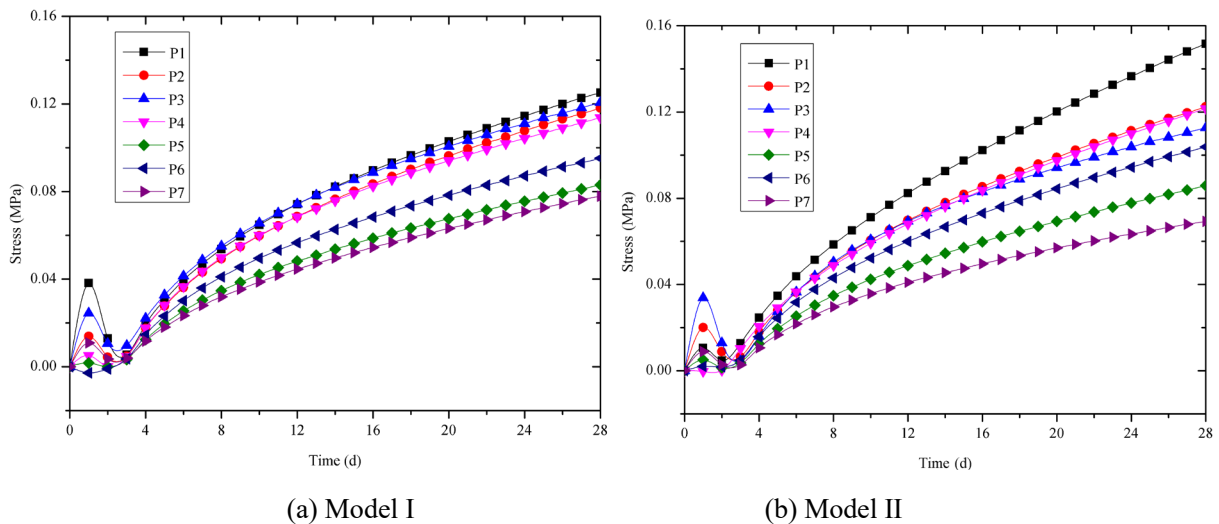

(a) Model I   (b) Model II

Fig.22. Major principal stress histories at the feature points under the combined factors

(a) Model I   (b) Model II
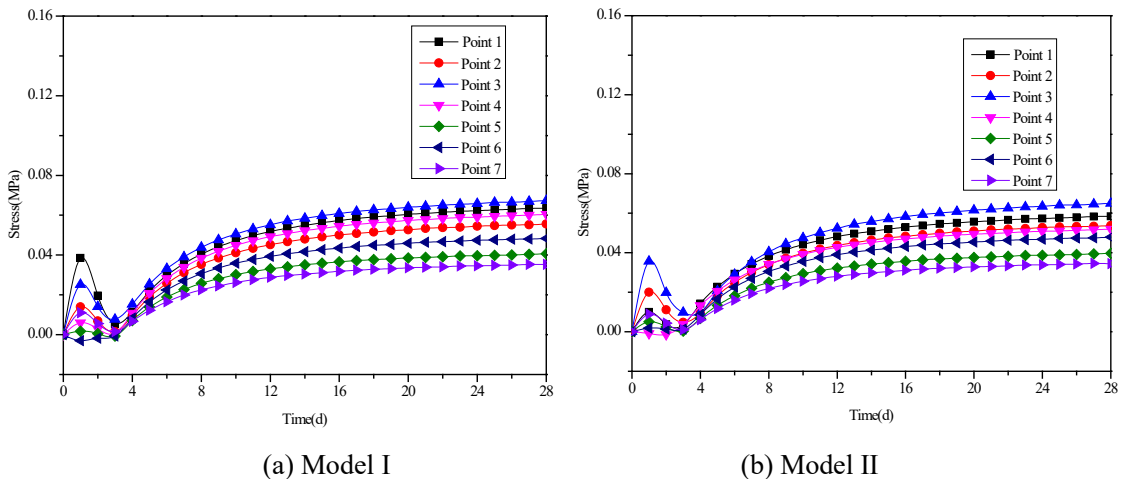
Fig.23. Major principal stress histories at the feature points under the temperature factor
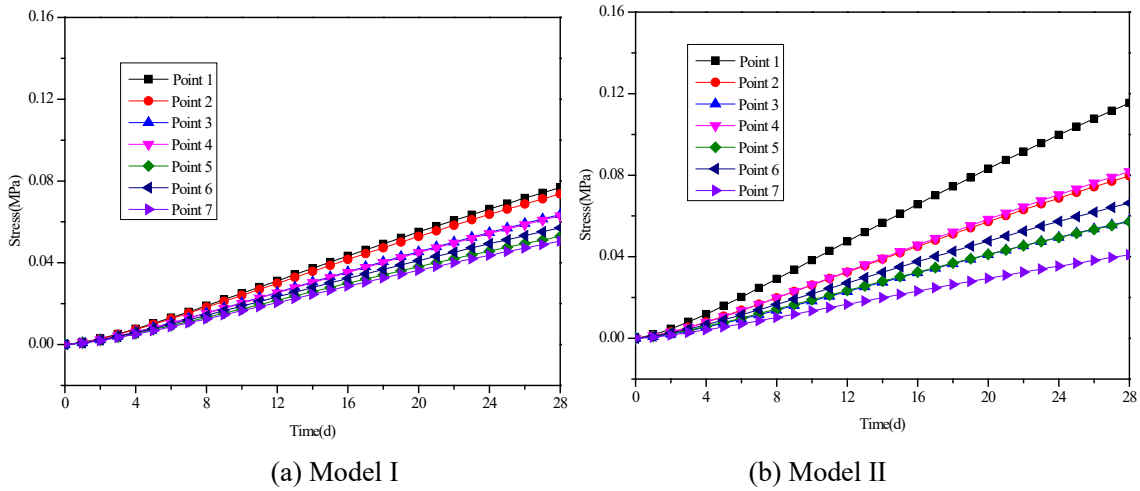

(a) Model I

(b) Model II

Fig.24. Major principal stress histories at the feature points under the autogenous volume deformation factor

5.4. The effect of aggregate orientation on the mechanical behavior

The effect of aggregate orientation should be considered for the non-spherical aggregate. Thermo-mechanical analysis is performed on the rotated crushed aggregate models (Model II~ Model V) by using the diffuse meshing method. The resulting major principal stress contours in 1 d and 28 d are given in Fig.25 and Fig.26, respectively. It can be found qualitatively that the stress distribution in most mortar regions is virtually unchanged. However, for the region with sparsely distributed aggregate, the locations of stress concentration basically rotates with the orientation of the crushed aggregate and always locate at the sharp corners of the crushed aggregates. This is because orientation of aggregate in different models changes the distance between aggregates, and the results indicate that the orientation of the aggregate plays a decisive role in the areas with sparsely distributed aggregate, where the interaction between the aggregate and the mortar is stronger than that of between aggregate to aggregate. However, the influence of the orientation of aggregate is reduced in the regions with compact distributed aggregate.
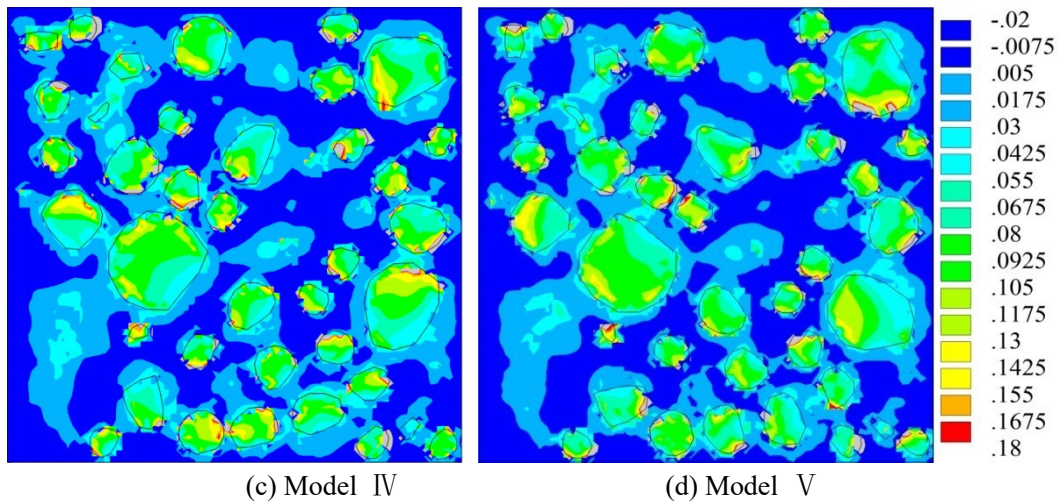

(a) Model II

(b) Model III

<div align="center">(c) Model Ⅳ   (d) Model Ⅴ</div>
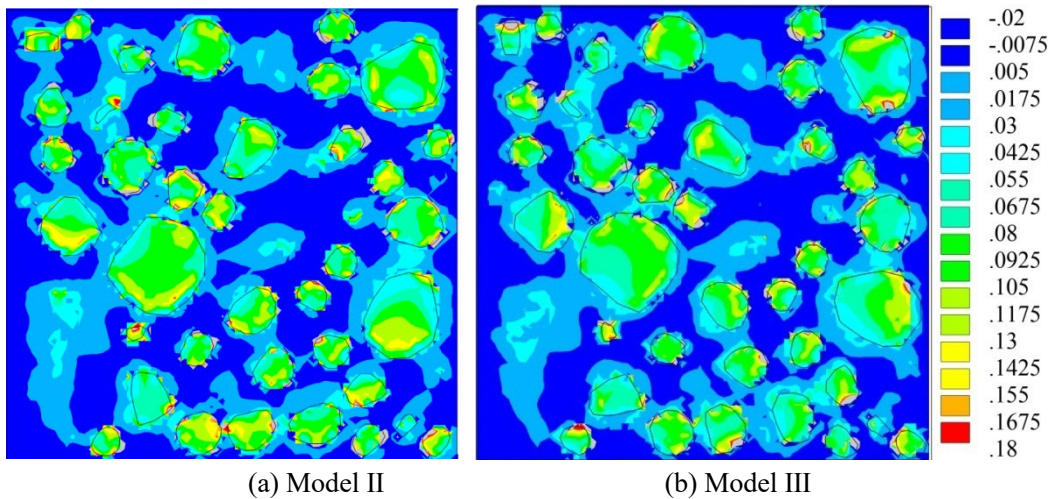
<div align="center">Fig.25. Comparison of major principal stress contours (1d), MPa</div>

<div align="center">(a) Model II   (b) Model III</div>

<div align="center">(c) Model Ⅳ   (d) Model Ⅴ</div>
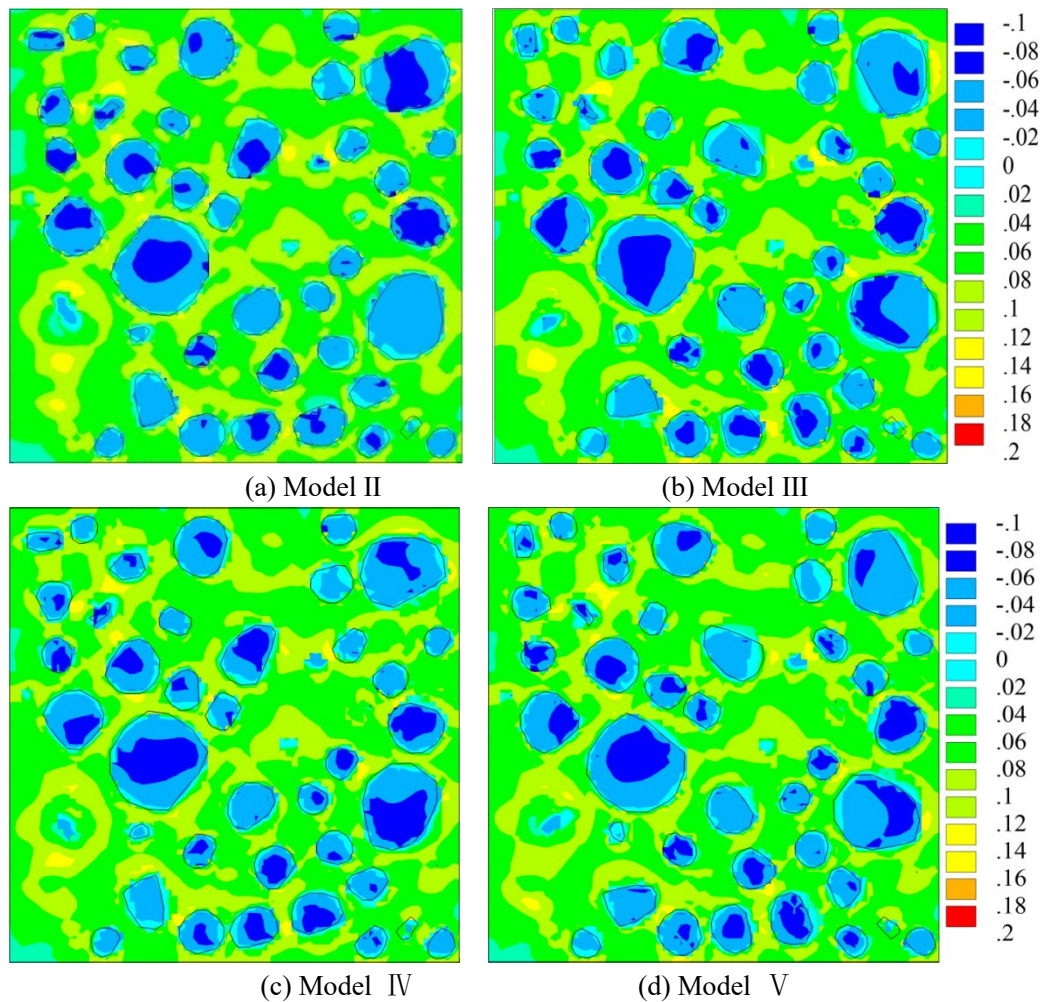
<div align="center">Fig.26. Comparison of major principal stress contours (28d), MPa</div>

Fig.27 is the maximum principal stress envelope of the four models through entire simulated process. The four curves have almost the same trend and have little difference in value during curing. Compared the rotation models to the reference one (Model II), the largest relative stress difference occurs at the initial stage of casting where the temperature gradient and elastic modulus of mortar vary up to 1.7%, which is far less than the relative stress difference caused by the aggregate morphology (6.5%).
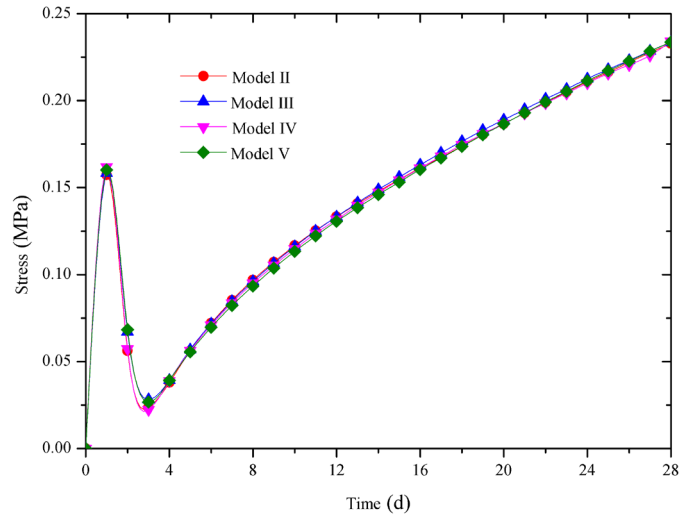
<div align="center">2</div>

Fig.27. Comparison of the maximum principal stress envelopes

In summary, the orientation of aggregates has little effect on the macro-mechanical properties of concrete, but it has a certain influence on the spatial distribution of self-restrained stress. The results also reflect to some extent that the distribution of initial damage of concrete is not completely random, but closely related to the orientation of aggregates. Therefore, as far as internal crack (damage) initiation is concerned, the reliability of numerical simulation results highly depends on the accuracy of the mesoscopic model of concrete, which needs accurate description of aggregate orientation. However, for studying macroscopic properties of concrete, orientation of aggregate is not a significant concern.

6. Conclusions

In this paper, a thermo-mechanical model with regular-element discretization is presented by combing the diffuse meshing technology with the linear viscoelasticity. This model can effectively reduce the difficulties in grid discretization of concrete, especially when the aggregates are complex-shaped, and provide an reliable approach to calibrate mesoscopic properties of the multiphase material. The proposed model has the accuracy comparable to the results from the three-phase model with exact meshing method, while requires only diffuse elements of regular shape. The mechanism of the self-restraint stress in concrete during curing, as well as the effect of aggregate morphology and orientation on the thermal-mechanical behavior of concrete, are investigated. The cross-scale simulations for adiabatic temperature rise, creep and autogenous volume deformation were preformed, respectively, and compared, which confirmed that the proposed approach could be used for mesoscale thermo-mechanical simulations. The proposed approach can also be used as a tool for parameter calibration of mesoscopic models. The main conclusions from the work are summarized below.

(1) The morphology and orientation of aggregate have little effect on the thermal development of concrete. The content of cement mortar is the main factor affecting the internal temperature field of concrete.

(2) The stresses produced inside the cement mortar during temperature rising are compressive and transferred to tensile during cooling. Due to the thermo-mechanical mismatch between different phases, the heterogeneity causes stress concentrations near the interface.

(3) The impact of aggregate morphology mainly affects the process of temperature rising. Orientation of aggregate has little effect on the overall response of concrete but affects local spatial distribution of self-restraint stress due to distance alternation and sparsity of aggregate.

(4) Though reasonably good results were obtained by the diffuse meshing method without considering the

physics of the ITZ, Further investigations on the effects of ITZ on the local properties of concrete are required and can be done by extending the current diffuse meshing model to cover three phases in one element. This future work will also include other thermal conditions, such as elevated temperature, and fracture of concrete subject to residual self-restraint stress at the end of curing.

Ete under other thermal conditions (i.e. elevated temperature) and investigating the effects of volume content, gradation and shape parameters of aggregate will be studied in a future work. Since concrete will produce residual self-restraint stress at the end of curing, future study will concentrate on the fracture behavior of concrete under this initial stress filed.

Acknowledgements

References

[1] B.F. Zhu, Thermal Stresses and Temperature Control of Mass Concrete, Butterworth-Heinemann, Waltham, 2014.

[2] C.U. Grosse, M. Ohtsu, Acoustic Emission Testing, Springer-Verlag, Berlin Heidelberg, 2008.

[3] Y. Li, L. Nie, B. Wang, A numerical simulation of the temperature cracking propagation process when pouring mass concrete, Autom. Constr. 37 (2014) 203–210.

[4] Y. Xu, S.H. Chen, A method for modeling the damage behavior of concrete with a three-phase mesostructure, Constr. Build. Mater. 102 (2016) 26-38.

[5] F.H. Wittmann, P.E. Roelfstra, H. Sadouki, Simulation and analysis of composite structures, Mater. Sci. Eng. 68 (2) (1985) 239–248.

[6] P.E. Roelfstra, H. Sadouki, F.H. Wittmann, Le béton numérique, Mater. Struct. 18 (1985) 327–335.

[7] F.H. Wittmann, H. Sadouki, T. Steiger, Experimental and numerical study of effective properties of composite materials, in: Micromechanics of Concrete and Cementitious Composites, Presses Polytechniques et Universitaires Romandes, Lausanne, 1993, pp. 59–82.

[8] J. Leite, V. Slowik, H. Mihashi, Computer simulation of fracture processes of concrete using mesolevel models of lattice structures, Cem. Concr. Res. 34 (6) (2004) 1025–1033.

[9] M.G. Alexander, Aggregates and the deformation properties of concrete, ACI Mater. J. 93 (6) (1996) 569–577.

[10] C. Zhou, B. Huang, X. Shu, Micromechanical model for predicting coefficient of thermal expansion of concrete, J. Mater. Civ. Eng. 25 (9) (2013) 1171–1180.

[11] Y.F. Fu, Y.L. Wong, C.S. Poon, C.A. Tang, Numerical tests of thermal cracking induced by temperature gradient in cement-based composites under thermal loads, Cement Concr. Compos. 29 (2) (2007) 103–116.

[12] G. Xotta, G. Mazzucco, V.A. Salomoni, C.E. Majorana, K.J. Willam, Composite behavior of concrete materials under high temperatures, Int. J. Solids Struct. 64 (2015) 86–99.

[13] F. Zunino, J. Castro, M. Lopez, Thermo-mechanical assessment of concrete microcracking damage due to early-age temperature rise, Constr. Build. Mater. 81 (2015) 140–153.

[14] S. Sinaie, A. Heidarpour, X.L. Zhao, A micro-mechanical parametric study on the strength degradation of concrete due to temperature exposure using the discrete element method, Int. J. Solids Struct. 88–89 (2016) 165–177.

[15] Y. Xu, Q. Xu, S.H. Chen, X.X.Li, Self-restraint thermal stress in early-age concrete samples and its evaluation, Constr. Build. Mater. 134 (2017) 104-115.

[16] T.D. Nguyen, D.T. Pham, M. N. Vu, Thermo-mechanically-induced thermal conductivity change and its effect on the behaviour of concrete, Constr. Build. Mater. 198 (2019) 98-105.

[17] A. Caggiano, G. Etse, Coupled thermo–mechanical interface model for concrete failure analysis under high temperature, Comput. Methods Appl. Mech. Engrg. 289 (2015) 498–516.

[18] A. Caggiano, D.S. Schicchi, G, Etse, M. Ripania, Meso-scale response of concrete under high temperature based on coupled thermo-mechanical and pore-pressure interface modeling, Eng. Fail. Anal. 85 (2018) 167–188.

[19] F. Bernachy-Barbe, B. Bary, Effect of aggregate shapes on local fields in 3D mesoscale simulations of the concrete creep behavior, Finite Elem Anal Des. 156 (2019) 13-23.

[20] X.Wang, Z.H. Nie, J. Gong, Zhenyu Liang, Random generation of convex aggregates for DEM study of particle shape effect. 268 (2021) 121468.

[21] S. Naderi, M. Zhang, An integrated framework for modelling virtual 3D irregulate particulate mesostructure, Powder Technol. 355 (2019) 808–819.

[22] Gomes, A, Voiculescu, I, Jorge, J, Wyvill, B, Galbraith, C. Implicit Curves and Surfaces: Mathematics, Data Structures and Algorithms. Springer Science & Business Media 2009.

[23] H.K Zhao, S. Osher, B. Menman, M. Kang. Implicit and Non-Parametric Shape Reconstruction from unorganized data using a variational level set method. Computer Vision and Image Understanding. (2006) 295~310.

[24] P. Wriggers, S.O. Moftah, Mesoscale models for concrete: homogenisation and damage behaviour, Finite Elem. Anal. Des. 42 (7) (2006) 623 – 636.

[25] Y. Huang, Z. Yang, W. Ren, G. Liu, C. Zhang, 3D meso-scale fracture modelling and validation of concrete based on in-situ X-ray Computed Tomography images using damage plasticity model, Int. J. Solids Struct. 67 – 68 (2015) 340 – 352.

[26] H. Edelsbrunner, N.R. Shah, Incremental topological flipping works for regular triangulations, Algorithmica 15 (3) (1996) 223 – 241.

[27] J. Bernal, REGTET: A Program for Computing Regular Tetrahedralizations, Computational Science – ICCS 2001, Springer, Berlin Heidelberg, 2001.

[28] X.N. Qin, C.S. Gu, C.F. Shao, X. Fu, L. Vallejo, Y. Chen, Numerical analysis of fracturing behavior in fully-graded concrete with oversized aggregates from mesoscopic perspective, Constr. Build. Mater. 253 (2020) 119184

[29] A. Gangnant, J.Saliba, C.L. Borderie, S.Morel, Modeling of the quasibrittle fracture of concrete at meso-scale: Effect of classes of aggregates on global and local behavior, Cem. Concr. Res. 89 (2016) 35 – 44.

[30] M.Q. Thai, T. Nguyen-Sy, J. Wakim, M.N. Vu, Q.D. To, T.T. Nguyen, A robust homogenization method for ageing and non-ageing viscoelastic behavior of early age and hardened cement pastes, Constr. Build. Mater. 264 (2020) 120264.

[31] T. Nguyen-Sy, T.K. Nguyen, V.D. Dao, K. Le-Nguyen, N.M, Vu, Q.D. To, T.D. Nguyen, T.T. Nguyen, A flexible homogenization method for the effective elastic properties of cement pastes with w/c effect, Cem. Concr. Res. 134 (2020) 106106.

[32] T. Nguyen-Sy, T.K. Nguyen, K. Le-Nguyen, N.M, Vu, A Simple yet Accurate Homogenization Method for Early Age Cement Pastes, J. Adv. Concr. Technol. 19 (2021) 630-643.

[33] T.W. Sederberg, J. Zheng, Bakenov, A. Nasri. T-splines and T-NURCCS, ACM Trans. Graphics. 22 (3) (2003) 477-484.

[34] W.H. Tong, Y.Y. Feng, F.L. Chen. A surface reconstruction algorithm based on implicit T-spline surfaces. Journa of Computer-Aided Desgin& Computer Graphics .18 (3) (2006):358-365 (in Chinese).

[35] Y. Liu, Y.Z. Song, Z.W. Yang, J.S. Deng. Implicit surface reconstruction with total variation regularization. Comput. Aided Geom. 52-53 (2017) 135-153.

[36] H.F. Ma, W.X. Xu, Y.C. Li, Random aggregate model for mesoscopic structures and mechanical analysis of fully-graded concrete. Comput Struct. 177 (2016) 103–113.

[37] X.W. Tang, C.H. Zhang. Layering disposition and FE coordinate generation for random aggregate arrangements. Journal of Tsinghua University (Science & Technology). 48 (12) (2008) 2048-2052 (in Chinese).

[38] W.J. Qiu, S.J. Fu, J.Q. Ye. Auto-generation methodology of complex-shaped coarse aggregate set of 3D concrete numerical test specimen, Constr. Build. Mater. 217 (2019) 612-625.

[39] P.K. Mehta, P.J. Monteiro, Concrete: Microstructure, Properties, and Materials, third ed., McGraw-Hill, New York, 2006.

[40] S.H. Chen, Hydraulic Structures, Springer-Verlag, Berlin Heidelberg, 2015.

[41] F. Incropera, D. DeWitt, Introduction to Heat Transfer, fourth ed., John Wiley & Sons, New York, 2002.

[42] J. Conceição, R. Faria, M. Azenha, F. Mamede, F. Souza, Early-age behaviour of the concrete surrounding a turbine spiral case: monitoring and thermomechanical modeling, Eng. Struct. 81 (2014) 327–340.

[43] Y. Yuan, Z.L. Wan, Prediction of cracking within early-age concrete due to thermal, drying and creep behavior, Cem. Concr. Res. 32 (7) (2002) 1053–1059.

[44] S.J. Fu, T. He, G.J. Wang, S.H. Zhang, L.C. Zou, S.H. Chen, Evaluation of cracking potential for concrete arch dam based on simulation feedback analysis, Sci. China Technol. Sci. 54 (3) (2011) 565–572.

[45] T. N' Guyen, Apport de la modélisation mésoscopique dans la prédiction deséccoulements dans les ouvrages en béton fissuré en conditions d' accident grave (Ph.D. thesis), Pau, 2010.

[46] Z. Song, Y. Lu. Mesoscopic analysis of concrete under excessively high strain rate compression and implications on interpretation of test data. Int. J. Impact. Eng.,46 (2016) 41-55.

[47] F. Grondin, H. Dumontet, A.B. Hamida, H. Boussa, Micromechanical contributions to the behaviour of cement-based materials: Two-scale modelling of cement paste and concrete in tension at high temperatures, Cem. Concr. Compos. 33 (3) (2011) 424–435.

[48] H.Q. Yang, W.W. Li, Hydraulic Concrete Research and Application, China Water and Power Press, Beijing, 2005 (in Chinese).

[49] B. Sun, Z. Li, Adaptive concurrent multi-scale FEM for trans-scale damage evolution in heterogeneous concrete, Comput. Mater. Sci. 99 (2015) 262–273.

[50] S.H. Chen, Computational Rock Mechanics and Engineering, China Water Power Press, Beijing, 2006 (in Chinese).

[51] S.H. Chen, G.N. Pande, Rheological model and finite element analysis of jointed rock masses reinforced by passive, fully-grouted bolts, Int. J. Rock Mech. Mining Sci. Geomech. Abstr. 31 (3) (1994) 273–277.

[52] G. Xotta, V.A. Salomoni, C.E. Majorana, Thermo-hygro-mechanical meso-scale analysis of concrete as a viscoelastic-damaged material, Eng. Comput. 30 (5) (2013) 728–750.

[53] I. Lyse, Shrinkage and Creep of Concrete, ACI J. 31 (8) (1960) 775–782.

[54] J.P. Zhou, L.C. Dang, Handbook of Hydraulic Structure Design (Vol 5)-Concrete Dams, second ed., China Water and Power Press, Beijing, 2011 (in Chinese).

[55] Neville A M, Creep of concrete as a function of its cement paste content. Mag. Concrete. Res. 16 (46) (1964).:21-30.

[56] Y. Lee, M.S. Choi, S.T. Yi, J.K. Kim, Experimental study on the convective heat transfer coefficient of early-age concrete, Cem. Concr. Compos. 31 (1) (2009) 60–71.